Fakultät für Physik und Astronomie

Ruprecht-Karls-Universität Heidelberg

Diplomarbeit

Im Studiengang Physik

vorgelegt von

Dominic Wörner

geboren in Hardheim

2011

Nichtlokale Anfangszustände und Korrelationen beim Anregungstransport im FMO Komplex

Die Diplomarbeit wurde von Dominic Wörner

ausgeführt am

Max-Plack-Institut für Kernphysik

unter der Betreuung von

Herrn Priv.-Doz. Dr. Jörg Evers

Department of Physics and Astronomy

University of Heidelberg

Diploma thesis

in Physics

submitted by

Dominic Wörner

born in Hardheim

2011

Non-local Initial States and Correlations in the Excitation Transport of the FMO Complex

This diploma thesis has been carried out by Dominic Wörner

at the

Max-Planck-Institute for Nuclear Physics

under the supervision of

Priv.-Doz. Dr. Jörg Evers

Nichtlokale Anfangszustände und Korrelationen beim Anregungstransport im FMO Komplex :

In dieser Arbeit untersuchen wir den Anregungstransfer während der Fotosynthese im Fenna-Matthews-Olson Komplex. Wir beschreiben diesen mit Hilfe einer phänomenologischen Liouville-von-Neumann Gleichung in Lindbladform. Im ersten Teil der Arbeit widmen wir uns dem Einfluss nichlokaler Anfangszustände auf die Transporteffizienz. Dabei ermitteln wir unter anderem jene nichtlokalen Anfangszustände, die bei kohärenter Zeitenwicklung zu maximaler Transporteffizienz führen und stellen fest, dass diese ihre hohe Effizienz auch unter dem Einfluss von Dephasierung über einen großen Bereich von Dephasierungsraten erhalten. Darüber hinaus disktuieren die Möglichkeit, dass die Anregung den Komplex über ein anderes Pigment als üblich verlässt. Im zweiten Teil der Arbeit beschäftigen wir uns mit dem Auftreten von Korrelationen zwischen den Eintritts- uns Ausgangspigmenten, initiiert durch die im ersten Teil bestimmten Anfangszustände. Dazu nutzen wir die Klassifizierung durch Verschränkung, "Quantum Discord" und Wechselseitiger "Mutual" Information. Wir finden heraus, dass die Dynamik, ausgehend von den hoch effizienten Anfangszuständen mit mehr Korrelationen einhergeht als die der niedrig effizienten. Außerdem stellen wir einen Zusammenhang zwischen den Quantenkorrelationen und einem einfachen Kohärenzmaß, sowie zwischen den klassischen Korrelationen und der quantenmechanischen Reinheit eines Teilsystems her. Diesen Beobachtungen geht ein Beweis der Äquivalenz der relativen Verschränkungsentropie und dem Quantum Discord im Null- und Einanregungsraum voraus. Abschließend gehen wir kurz auf die Möglichkeit doppelter Anregungen ein und diskutieren dabei die Auswirkung von Kohärenzen im Anfangszustand auf die Entwicklung von Korrelationen.

Non-local Initial States and Correlations in the Excitation Transport of the FMO Complex:

In this thesis, we investigate the excitation energy transfer process during photosynthesis in the Fenna-Matthews-Olson complex described by a phenomenological Liouville-von-Neumann equation in Lindblad form. In the first part, we focus on the effect of non-local superpositions in the initial excitations on the transport efficiency. We identify those non-local initial states that exhibit maximum efficiency for zero dephasing and find that the efficiency is robust over a broad regime of dephasing rates. In addition, we discuss the advantage of a trapping (exit) site other than the usual choice. In the second part, we investigate the correlations between the entry sites and the exit sites in terms of entanglement, quantum discord and mutual information for initial states found in the first part. We see that the high efficiency states show more correlations than the low efficiency states and recognize a connection between quantum correlations and a simple coherence measure. Furthermore, the structure of classical correlations is found to be related to a quantity based on the purity of a subsystem. Besides that, we give a proof of the equivalence of the relative entropy of entanglement and quantum discord in the zero- and single-excitation subspaces under assumptions valid in this model. Finally, we briefly investigate the effect of initial coherence on the correlations in a straightforward extension to higher excitations.

Contents

1 Introduction

During the last few years, a new field of research, *Quantum Biology* Arndt *et al.* (2009); Ball (2011), has emerged. The topics range from the avian compass, which allows birds to sense subtle changes of the Earth's magnetic field Gauger *et al.* (2011), to the highly efficient energy transfer during photosynthesis. But what is it that makes biology quantum? For the avian compass, quantum information theory applied to the widely accepted radical pair model predicts entanglement between two spatially separated electron spins of molecules located at the back of the bird's eye persisting for up to hundreds of microseconds. In the case of photosynthesis, there had been experiments that caused a change of paradigm. Traditionally the excitation transfer in photosynthetic units was described by an incoherent rate equation, where the rates were calculated by Fermi's golden rule Förster (1948). But sophisticated nonlinear spectroscopy techniques have found evidence of wave-like behavior or, more precisely, quantum coherence between excitonic states at cryogenic Brixner *et al.* (2005); Engel *et al.* (2007) and even at physiological temperature Collini *et al.* (2010); Panitchayangkoon *et al.* (2010). If the socalled quantum beats (cf. Sec. 2.2) observed in the spectra are really caused by quantum coherence, then the incoherent theory is not sufficient to describe the transport process and a true quantum mechanical theory has to be applied. This opens new paths to understand the extraordinary near unit efficiency of excitation transfer from the antenna complex, where the solar photons are being harvested, to the reaction center, where the charge separation and the conversion to chemical energy takes place. Although our interest is focused only on this transport phenomenon, we formulate the key questions driving the whole field:

How can quantum phenomena, like entanglement and quantum coherence, occur in such warm and wet environments, and do they play a vital role in the biological function and

are thus a product of natural evolution?

Answering these questions could pave the way for new kinds of quantum technology like ultra-efficient solar cells or eventually a quantum computer.

Entanglement, which Schrödinger (1935) called *the characteristic trait of quantum mechanics*, is a manifestation of quantum correlations and wires together subsystems in such a manner that we have to describe them as a whole, even if they are spatially separated. This phenomenon can be used as a valuable resource to accomplish certain tasks in a way that is impossible in classical physics. Among them, we can mention quantum cryptography Ekert (1991), quantum search Grover (2001) and quantum teleportation Bennett *et al.* (1993). In the past years, also quantum correlations beyond entanglement have been identified. The most popular, quantum discord Ollivier and Zurek (2001), already proved to be sufficient for quantum computation Datta and Shaji (2008); Merali (2011), and almost every quantum system possesses it Ferraro *et al.* (2010). Moreover, for a long time it was thought that entanglement can only occur if the interaction between the subsystems is stronger than the thermal energy due to the coupling to the environment. A situation that is typically only given for ultra-low temperatures. This, however, turned out to be wrong. Galve *et al.* (2010) showed that entanglement can also persist at high temperatures, if the environment is driven out of thermal equilibrium (see also Vedral (2010)). A similar effect was recognized by Briegel and Popescu (2008). In this paper, they argued that in open driven systems far from equilibrium, error correction can occur which can maintain entanglement. Furthermore, Nalbach *et al.* (2010) pointed out that spatially correlated fluctuations of the environment can preserve coherence in a dimer. Therefore, it is probable that the environment of the light-harvesting pigment's electronic system, which typically consists of the nuclear movement due to interaction with the protein scaffold and solvent, plays a crucial role. Unfortunately, experiments that reveal detailed information of the environment are missing, and the vast number of degrees of freedom makes it extremely hard to perform accurate quantum mechanical calculations from microscopic grounds. For this reason, the traditional approach to tackle open quantum systems is to derive a quantum master equation by tracing out the environmental degrees of freedom, assuming weak system-environment coupling and a large environment without memory. This leads to the Redfield (1957) theory, but the approximations are in general not justified Ishizaki and Fleming (2009a). Today's reference theory was derived by Ishizaki and Fleming (2009b). It uses the Gaussian property of phonon operators in order to build up a hierarchy of coupled equations of motion (HEOM). This theory is able to inter-

polate between Förster's and Redfield's theory, but is only practical for special spectral densities and is computationally expensive. Kreisbeck *et al.* (2011) proposed that the approach is suitable for the usage of graphics processing units which can lead to a tremendous decrease of computation time. Nalbach *et al.* (2011) used a path integral method (QUAPI) whose results coincide with the former approach, but is likewise costly. A very recent method by Ritschel *et al.* (2011), based on the non-Markovian quantum state diffusion approach, showed also good agreement with the HEOM, and can be solved within minutes on a standard PC. In addition, it was pointed out that in principle, complicated structured spectral densities can be implemented, but the investigations have just started. Besides that, also a more pragmatic, phenomenological ansatz turned out to be fruitful. There, the coupling to the environment is simulated by adding Lindblad superoperators to the Liouville-von-Neumann equation. These guarantee a positive and trace preserving, though non-unitary, evolution of the system's density matrix. Using such a model, the phenomenon of noise-assisted transport was recognized by Plenio and Huelga (2008) and Mohseni *et al.* (2008a). The basic idea thereby is the interplay of coherent dynamics and noise to circumvent their respective disadvantages for excitation transfer. Moreover, the occurrence of non-classical behavior, in form of entanglement Caruso *et al.* (2010); Fassioli and Olaya-Castro (2010), violation of Leggett-Garg inequalities Wilde *et al.* (2010), and quantum discord Brádler *et al.* (2010), was investigated.

If we take up the main questions from above again, we realize that we have reviewed some suggestions to answer the first one, concerning the *existence* of quantum behavior. But there is no definite answer of which is *the* ingredient that leads to preservation of quantum behavior. Maybe there is no single answer and the interplay of different effects is responsible. For the second part of the question, concerning the *role* of the effects, the situation is even more involved. Plenio and Huelga (2008) pointed out that efficient transport is incompatible with fully coherent evolution, and Fassioli and Olaya-Castro (2010) even showed an inverse relationship between entanglement and efficiency. In contrast, Scholak *et al.* (2011) concluded that efficient transfer is connected with the build-up of strong intersite entanglement. Furthermore, all of these studies were performed under the assumption that there is at most one excitation present. In this scenario, quantum coherence, entanglement and also correlations beyond, as measured by quantum discord, are closely related to each other as we will see later. Therefore, it is impossible to ascribe distinct functional roles to them.

In this thesis, we will follow the latter, phenomenological ansatz to describe the excitation

transport in a molecular aggregate, the Fenna-Matthews-Olson (FMO) complex, which is part of the light-harvesting unit in certain bacteria. We take the view that there are general features which can already be identified in the less realistic models, and trade the realism with the possibility to investigate a broad parameter regime. The results can then be approved within more sophisticated frameworks as discussed above.

The main questions that drive us throughout this thesis can be summarized as follows:

Can quantum superpositions of localized initial excitations affect the transport efficiency, and is this connected to the appearance of quantum correlations between the entry and exit sites?

On this journey, of course, other questions arise, which lead to surprising insights. These, as well as the content of this thesis in general, will be briefly previewed in the remainder of this introduction.

In Chapter 2, we introduce the FMO complex. We present its structure (Sec. 2.1), discuss its role in the photosynthesis and review recent experiments which suggested the quantum behavior (Sec. 2.2). After that, we construct the theoretical model in Chapter 3 on a phenomenological basis, rather than from a microscopic derivation. In the end, we arrive at a Markovian quantum master equation in Lindblad form and discuss its validity. With the model at hand, we proceed to a discussion of the efficiency of the excitation transfer in Chapter 4. There, the focus is on the interplay of specific initial superpositions and the trapping process which passes the excitation to the next unit, the reaction center. We find out that there exist superpositions of the entry sites allowing highly efficient excitation transfer over a large regime of dephasing rates and is therefore robust against noise. We recognize that in the network model of the FMO complex, another trapping site could be more beneficial and motivate this observation by looking at a connectivity measure. Chapter 5 is dedicated to the study of entanglement and correlations in general. A rather new measure of quant um correlations, quantum discord, which in general reaches beyond entanglement is introduced (Sec. 5.1.2). We prove that under assumptions valid in our model the quantum discord is equivalent to the relative entropy of entanglement (Sec. 5.2). After these formal considerations we follow the dynamics of quantum and classical correlations between the subsystems, consisting of the entry and the trapping sites of the network, for initial conditions we have identified to lead to optimal respective pessimal efficiency (Sec. 5.3). We see that the correlations, especially the quantum correlations, are greater if the transfer is more efficient. Strikingly, we are able to relate the quantum

correlations to a measure of coherence between the two subsystems, as well as the classical correlations to the purity of a subsystem's density matrix. In the end (Sec. 5.4), we briefly discuss the effect of the most simple incorporation of double-excitations on the dynamics of quantum discord and entanglement, quantified by the logarithmic negativity. In Chapter 6, we conclude with a summary and an outlook.

2 The Fenna-Matthews-Olson Complex

The Fenna-Matthews-Olson (FMO) complex is part of the photosynthetic unit of the green sulfur bacteria. Its functional role is the transport of excitation energy from the antenna complex, where photons are absorbed, to the reaction center (RC), where charge separation takes place and the excitation energy is converted into chemical energy. Despite the fact that it was the first antenna complex* whose X-ray structure was resolved in 1975 Fenna and Matthews (1975), it is still subject of active research. In this short introductory chapter, we first describe the structure of of the complex. This will be useful for understanding the theoretical model we introduce in the next chapter. After that, we present the technique of two-dimensional electronic spectroscopy and what we have already learned from these experiments which essentially fueled the present discussions of quantum behavior in light-harvesting complexes.

2.1 Structure

The FMO complex is a trimer with three identical subunits. Each monomer was, until recently, thought to consist of seven bacteriochlorophyll pigment molecules. Now it is suggested that there are eight Schmidt am Busch *et al.* (2011). But in our calculations we hold on to the seven site model. The actual type of pigment molecule depends on the species of green sulfur bacteria. The pigment molecules, later also called sites, are responsible for the excitation transport. They are embedded in a protein scaffold that causes an effective local environment for each individual pigment. The pigment-pigment interaction

*The FMO complex can be seen as part of the antenna, since it can also absorb photons.

can be approximated as of dipole-dipole type, since the intramonomer distances between pigments range from 4 Å to 11 Å. The closest intermonomer pigment-pigment distance is 24 Å, and the coupling is typically neglected Cheng and Fleming (2009). These numbers are from the time when the 8th pigment had not been discovered yet. It seems that this pigment is hard to assign to a monomer, since it is located between pigment 1 and 6 of two distinct monomers (see e.g. Fig. 1 in Hoyer *et al.* (2011)).

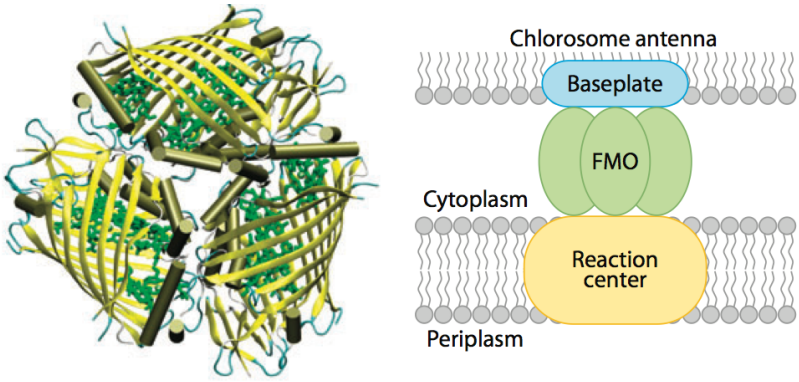

Figure 2.1: (Left) Top-view of the Fenna-Matthews-Olson (FMO) protein trimer from green sulfur bacterium *Prosthecochloris aestuarii*. The protein is depicted in yellow, and the bacteriochlorophyll (BChl) molecules are in green. (Right) The FMO complex is located between the photosynthetic antenna complex (chlorosome) and the reaction center. The Figure is taken from Cheng and Fleming (2009).

While the structure is now known to a precision of the order of 1 AA, the orientation of the whole complex can not be resolved completely by optical experiments. Since calculations of environmental dielectric effects by Louwe *et al.* (1997) and Adolphs and Renger (2006); Adolphs *et al.* (2008) indicate that the site energies of site 3 and 4 are downtuned, whereas the site energies of pigments 1,6 (and 8) are shifted to higher values, it is assumed that the former are located near the RC, while the latter are close to the antenna (see Fig. 2.2). Recent mass spectroscopy experiments support this assumption Wen *et al.* (2009).

2.2 Transport Pathways and Quantum Effects

With the advent of two-dimensional electronic spectroscopy, a nonlinear technique based on the photon echo spectroscopy, it became possible to examine the ultrafast excitation transport on the femtosecond timescale. The experimental procedure can be summarized

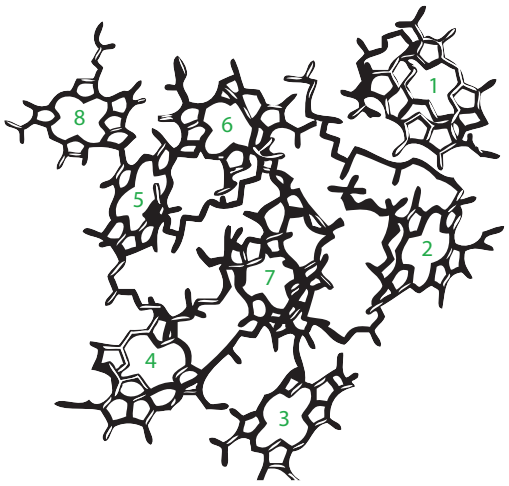

Figure 2.2: Distribution of the pigments within a single monomer. Pigments 1 and 6 (and 8) are assumed to be close to the antenna complex, whereas pigments 3 and 4 are located near the RC. The Figure has been created with PyMOL.

as follows. The sample is hit by three successive ultrashort laser pulses with variable time delays. Then the amplitude and phase of the fluorescence signal is measured in the phase matching direction $k_s = -k_1 + k_2 + k_3$ as a function of the three delay times[†]. After a two-dimensional Fourier transformation with respect to the delay times between the first and the second pulse, and the third and the signal, we have a set of two-dimensional spectra[‡]. Off-diagonal peaks in these spectra represent couplings between the excitons ($\Delta t = 0$) and energy transfer ($\Delta t > 0$).

Engel *et al.* (2007) showed that these off-diagonal peaks show a beating, when observed as a function of Δt. These *quantum beats*, which are an evidence of quantum coherence in the excitonic basis, were observed at 77 K for more than 600 fs. Later, these experiments were repeated at ambient temperature Panitchayangkoon *et al.* (2010) and other light-harvesting complexes Collini *et al.* (2010). Here, the beatings were observed at least up to 300 fs, and therefore could be important for the excitation transfer which takes place on this time scale. On the other hand, these two-dimensional spectra do not represent the actual density matrix as one is sometimes misled to think Abramavicius and Mukamel (2010). Thus, it is still required to rule out other processes which can lead to the same observed beatings. A more direct attempt to test for quantum behavior would be to look for violations of Bell-like Bell (1964) or Legget-Garg inequalities Leggett and Garg (1985); Wilde *et al.* (2010).

[†]Two between the three pulses plus the one between the last pulse and the fluorescence signal.
[‡]One for each delay time Δt between the second and the third pulse.

3 The Model

In this chapter, we give a concise introduction of the regimes of excitation transfer. Then, we build a phenomenological model and discuss the underlying assumptions. Furthermore, we briefly discuss a microscopic model that leads to the same equation of motion and provides a connection to the environmental temperature. This provides us with an idea of the parameter regime in which our model is applicable.

3.1 Regimes of Excitation Transport

We can distinguish three regimes of excitation transport (cf. e.g. May and Kühn (2011)). This classification is mainly given by the ratio of two different timescales, τ_{trans} and τ_{rel}. τ_{trans} is the typical timescale of the excitation transport without any disturbance, and is on the order of the inverse of a characteristic electronic coupling between the molecules. τ_{rel} is the time a molecule needs to relax to the vibrational ground state after an electronic excitation, and can be approximated by the timescale on which environmental correlations vanish.

If $\tau_{rel} \ll \tau_{trans}$, we can not write down a wave function that spreads over several molecules, and the excitation transport is comparable to a diffusion process or random walk. The theoretical description, in terms of incoherent rate equations, was formulated by Förster (1948).

On the other hand, if $\tau_{rel} \gg \tau_{trans}$, the electronic excitation has to be described by a delocalized exciton. Especially in the case of weak exciton-phonon coupling a description

of the exciton dynamics by a Quantum Master Equation (QME) is appropriate. In Fig. 3.1, you can see an illustration of the transport process in the two marginal regimes.

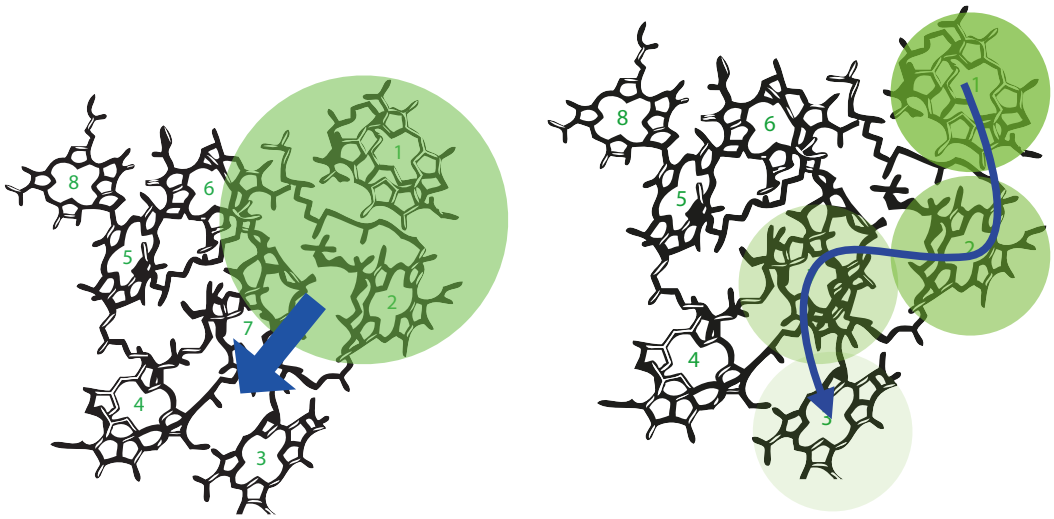

(a) Delocalized excitation moves through the complex as a wave.

(b) Incoherent diffusion of the localized excitation.

Figure 3.1: Illustration of the coherent and incoherent excitation transport through the FMO complex.

Of course, the third regime is where the two time scales are comparable, and it seems that for excitation transport in photosynthetic units this is exactly the case. Here, the electronic system and the motion of the molecules should be treated on the same footing. There has been a lot of effort to find frameworks which allow to simulate the dynamics in this regime efficiently Rebentrost *et al.* (2009); Ishizaki and Fleming (2009b); Huo and Coker (2010); Kreisbeck *et al.* (2011); Nalbach *et al.* (2011); Ritschel *et al.* (2011). Except for the last approach, all of them are computationally very expensive, and (yet) not suitable to investigate a broad parameter regime (see also the discussion in the Introduction). Here, we choose a framework that was originally developed to interpolate between both marginal regimes Haken and Strobl (1973). Instead of perturbative arguments, the theory is built-up on the assumption that the environmental interaction can be modeled by classical stochastic fluctuations. Therefore the question will be if this assumption is appropriate.

3.2 The Liouville-von-Neumann equation

This section is based on the derivation presented by Mohseni *et al.* (2008a). We start with a single electronic excitation. The Hamiltonian describing the system of n coupled two-level systems which represent electronic ground and first excited state, is known as tight-binding Hamiltonian May and Kühn (2011)

$$H_S = \sum_{i=1}^{n} \hbar\omega_j \left|i\right\rangle \left\langle i\right| + \sum_{i\leq j} \hbar v_{ij} (\left|i\right\rangle \left\langle j\right| + \left|j\right\rangle \left\langle i\right|). \tag{3.1}$$

The states $|i\rangle$ represent an excitation at site i. The site energies are denoted by $\hbar\omega_i$. In a molecular aggregate they usually differ from site to site. This is even true in the case of the FMO complex where the sites are identical molecules. The reason is the local environment which shifts the site energies due to electrostatic interaction. The v_{ij} are the couplings between sites i and j. Typically, these are given by the dipole-dipole interaction. In what follows, we will use the Hamiltonian published by Adolphs and Renger (2006) and discussed in Appendix A.1.

3.2.1 Haken-Strobl-Reineker Model and Pure Dephasing

We describe the coupling to the phonon bath solely as a stochastic modulation of the site energies. Fluctuations of the intermolecular couplings are typically smaller and are therefore neglected Cho *et al.* (2005); Adolphs and Renger (2006). The interaction Hamiltonian can then be written as

$$H_{int}(t) = \sum_i q_i(t) \left|i\right\rangle \left\langle i\right|, \tag{3.2}$$

where the $q_i(t)$ describe stochastic bath fluctuations. These random variables are taken to be unbiased Gaussian fluctuations, with $\langle q_i(t)\rangle$ = 0 and

$$\langle q_i(t) q_j(0)\rangle = \delta_{ij}\delta(t)\tilde{\gamma}. \tag{3.3}$$

Note that for Gaussian fluctuations, n-point correlations up to arbitrary large n can be decomposed into two-point correlations. This is the classical analog to Wick's Theorem, known from Quantum Field Theory. Therefore, the stochastic process is completely de-

termined by Eq. (3.3). Nevertheless, the assumptions inherent in Eq. (3.3) are very strong and restrictive. The Kronecker delta δ_{ij}, where $\delta_{ij} = 1$ for $i = j$ and zero else, denotes that the correlations are spatially uncorrelated, i.e. we have independent baths at each site. This assumption is justified by recent calculations Olbrich *et al.* (2010). The following delta distribution $\delta(t)$, which can here be seen as a continuous version of the Kronecker delta δ_{t0}, represents the so-called Markov approximation. Here, we assume that the memory time of the bath is short compared to the timescale on which the reduced system changes. Recent calculations for the autocorrelation function of the site energies show a decay that can be described by two exponentials (besides oscillations). The decay times of those can be interpreted as the memory time of the environment. There is a fast initial decay time of about 4-5 fs for all sites, while the slower decay time is 140 fs for sites 1-6 and 8, and 230 fs for site 7 Olbrich *et al.* (2011). We can estimate the timescale of the system by looking at the inverse of the largest coupling in the Hamiltonian (A.1), which is about 50 fs. This indicates that non-Markovian effects could be important. We postpone the discussion of the applicability of the model to the last paragraph in Sec. 3.2.1. The last assumption, equal coupling strengths at each site, can be relaxed without further implications in the final equation of motion which has the form of a Liouville-von-Neumann equation with a Lindblad term

$$\frac{\partial \rho(t)}{\partial t} = -\frac{i}{\hbar}[H_S, \rho(t)] + \mathcal{L}(\rho(t)). \tag{3.4}$$

The first term of the right-hand side of Eq. (3.4) describes the familiar coherent evolution of the system. Note that H_S is now averaged with respect to the fluctuations and should be denoted by $\langle H_S \rangle$. But since we assumed Gaussian fluctuations with zero mean, we have $\langle H_S \rangle = H_S$. The second term which describes the irreversible effects due to the interaction with the phonon bath is called Lindblad super operator. The term super operator stems from the fact that it is acting on the density operator, and not on the states. The Lindblad super operator of the Haken-Strobl-Reineker Model Haken and Strobl (1973), with only diagonal fluctuations, has the effect of pure dephasing and is given by

$$\mathcal{L}_{deph}(\rho) = \tilde{\gamma} \sum_i [A_i \rho A_i^\dagger - \frac{1}{2}\{A_i A_i^\dagger, \rho\}], \tag{3.5}$$

with the generators $A_i = |i\rangle\langle i|$. Introducing ladder operators for the two-level system $\sigma_i^+ = |i\rangle\langle 0|$ and $\sigma_i^- = |0\rangle\langle i|$, we can recast Eq. (3.5) in the form Chin *et al.* (2010)

$$\mathcal{L}_{deph}(\rho) = \gamma \sum_i [-\{\sigma_i^+ \sigma_j^-, \rho\} + 2\sigma_i^+ \sigma_i^- \rho \sigma_i^+ \sigma_i^-], \tag{3.6}$$

with $\gamma = \frac{\tilde{\gamma}}{2}$.

We pause for a moment to make two
Remarks:

1. As the name pure dephasing indicates, so far only the coherences of the density operator in site basis are directly affected by the presence of environmental phonons. To be precise, it leads to an exponential decay of the coherences.

2. If we look at the time evolution of the populations $\rho_{ii}(t) = \langle i|\,\rho(t)\,|i\rangle$, we see that after strong coherent oscillations driven by the Hamiltonian the final state is a uniform distribution over all sites (see Fig. 3.2). This is, of course, not ideal for transport to a specific site. The reason for that is the lack of a temperature in our formalism. Thus, the system does not relax to a thermal ground state. However, we will circumvent this problem in the next section (Sec. 3.2.2) by introducing a process that traps excitation locally.

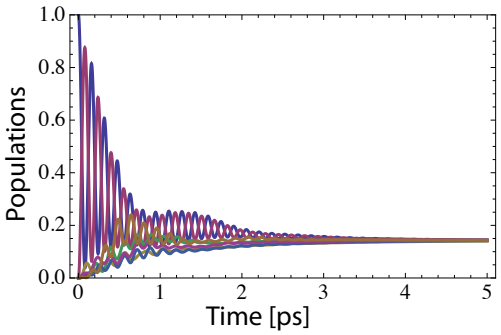

Figure 3.2: Evolution of the populations ρ_{ii} under the influence of pure dephasing (γ = 1 ps^{-1}).

Connection to Environmental Temperature

Even though we started with a temperature-independent ansatz of the fluctuations to arrive at a pure dephasing Lindblad term, it is possible to evoke a connection between the

dephasing rate and the temperature of the environment Mohseni *et al.* (2008b), and therefore with the experiments. We consider a standard spin-boson model (see e.g. Breuer and Petruccione (2007)) with an Ohmic spectral density with cut-off ω_c,

$$J(\omega) = \frac{E_R}{\hbar\omega_c}\omega e^{-\frac{\omega}{\omega_c}}. \tag{3.7}$$

We start with the QME for the full density matrix, assume that the initial state of the system and environment are uncorrelated and the environment is in thermal equilibrium. Then, we trace over the environmental degrees of freedom and end up with an equation of motion for the reduced density matrix of the system alone. The iterative solution of this equation leads to a perturbation expansion in the system-environment coupling strength, which is truncated at second order in the coupling (Born approximation). Thereafter, we can compare the equation with Eq. (3.4) and see that the dephasing rates in the Markovian regime are given by

$$\gamma = \pi\frac{kT}{\hbar}\frac{\partial J(\omega)}{\partial\omega}|_{\omega=0} = \pi\frac{kT}{\hbar}\frac{E_R}{\hbar\omega_c}. \tag{3.8}$$

For the FMO complex, we fix the reorganization energy and the cut-off frequency to E_R = $35\,\mathrm{cm}^{-1}$ Cho *et al.* (2005); Sarovar *et al.* (2010) and ω_c = $150\,\mathrm{cm}^{-1}$ Adolphs and Renger (2006). Note that of the $\hbar$ next to ω_c in Eq. (3.8) has already taken care, since ω_c is already given in the same units as E_R. The reorganization energy,

$$E_R = \int_0^\infty d\omega\,\frac{J(\omega)}{\omega}, \tag{3.9}$$

is often used as a measure for the coupling strength of the system to the environment Cheng and Fleming (2009). Following this mode of thought, we see that with a reorganization energy of $35\,\mathrm{cm}^{-1}$ and intersite couplings between 1 and $100\,\mathrm{cm}^{-1}$, the use of second-order perturbation theory, as used in the derivation above, seems not to be justified. But, since the reorganization energy is a global measure, its importance can be questioned. Indeed, Ritschel *et al.* (2011) showed that in many cases the reorganization energy is not a reasonable measure for the coupling strength. Thus, we can hope to justify the model, although we noticed that the reorganization energy and the intersite couplings are comparable. For this reason, we calculate the dephasing rates for T = 77 K and T = 277 K with Eq. (3.8), which represent the values of the experiments by Engel *et al.* (2007) and Panitchayangkoon *et al.* (2010),

$$\gamma_{77\,\mathrm{K}} \approx 7.4\,\mathrm{ps}^{-1} \qquad \gamma_{277\,\mathrm{K}} \approx 26.6\,\mathrm{ps}^{-1}. \tag{3.10}$$

It turns out that the results are remarkably close to the values found by fitting an exponential function to the decay of the quantum beats in the experiment by Panitchayangkoon *et al.* (2010). Tthey also found a linear connection between the dephasing rate and the temperature, with a proportionality factor of approximately 0.1^*. This relation was seen to hold for temperatures at least up to $150\,\mathrm{K}$. The next measuring point, $277\,\mathrm{K}$, deviates much, but also the error is large. Therefore, we can be confident that our model is applicable for dephasing rates up to $10\,\mathrm{ps}^{-1}$. Another note on the parameter regime is given in Appendix A.2.

3.2.2 Trapping and Exciton Recombination

We have seen that, so far, our model is not appropriate to describe an excitation transport process, since it leads to an equilibration of the populations. The critical process we have to include is a trapping process, i.e. an irreversible process that transfers the excitation from our system to a trap which represents the reaction center in a photosynthetic unit.

Since the net effect will be a decrease of our system's population, a straightforward incorporation is an anti-hermitian Hamiltonian of the form

$$H_{trap} = -i\hbar \sum_i \kappa_i \left|i\right\rangle \left\langle i\right|, \tag{3.11}$$

with local trapping rates κ_i. We note that an anti-hermitian Hamiltonian enters the Liouville-von-Neumann equation by an anti-commutator instead of a commutator. Further, under the impact of an anti-hermitian Hamiltonian, the trace of the density matrix is not conserved. This is obvious, because the purpose of the introduction was to model a decrease of the population. We can avoid this drawback by introducing an additional site which is only coupled to the system through the trapping process. Then the effect of Eq. (3.11) can also be recast into Lindblad form,

$$\mathcal{L}_{trap}(\rho) = \sum_i \kappa_i [2\sigma_{RC}^+ \sigma_i^- \rho \sigma_i^+ \sigma_{RC}^- - \{\sigma_i^+ \sigma_{RC}^- \sigma_{RC}^+ \sigma_i^-, \rho\}]. \tag{3.12}$$

Here, σ_{RC}^+ and σ_{RC}^- are the ladder operators corresponding to the additional site, representing the reaction center. This leads to a breakdown of the equipartitioning, we observed in the case of pure dephasing (Fig. 3.2), and is illustrated in Fig. 3.3.

*This means for T = 77 K they get a dephasing rate of $\gamma \approx 7.7\,\mathrm{ps}^{-1}$.

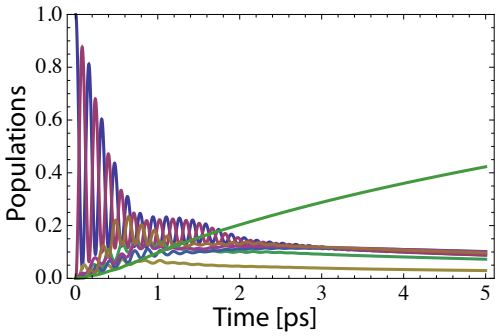

Figure 3.3: Evolution of the populations under the influence of pure dephasing ($\gamma = 1\,\mathrm{ps}^{-1}$) and local trapping at site 3 ($\kappa_3 = 1\,\mathrm{ps}^{-1}$). The increasing green line is the reaction center population.

We conclude our model with a term that takes care of the possibility that the excitation energy dissipates into the environment due to exciton recombination. The assumption of a large environment allows us to neglect the effect on the environment and we end up with the two equivalent formulations of either the anti-hermitian Hamiltonian

$$H_{diss} = -i\hbar \sum_i \Gamma_i \left|i\right\rangle \left\langle i\right| \tag{3.13}$$

or the Lindblad super operator

$$\mathcal{L}_{diss}(\rho) = \sum_i \Gamma_i [-\{\sigma_i^+ \sigma_j^-, \rho\} + 2\sigma_i^- \rho \sigma_i^+]. \tag{3.14}$$

The Γ_i are the local recombination rates, which are on the order of $1\,\mathrm{ns}$ for molecular aggregates Owens *et al.* (1987), and therefore do not play a role in the ultrafast excitation transfer, which happens on the (sub-) picosecond timescale.

We close this chapter by writing down the final form of the Quantum Master Equation in Lindblad form,

$$\frac{\partial \rho}{\partial t} = -\frac{i}{\hbar}[H_S, \rho] + \mathcal{L}_{deph}(\rho) + \mathcal{L}_{trap}(\rho) + \mathcal{L}_{diss}(\rho). \tag{3.15}$$

In the site representation, this is a system of coupled linear ordinary differential equations for the matrix elements ρ_{ij}, which can be solved numerically.

3.3 Conclusion

We introduced a phenomenological model of coupled two-level systems that represent the electronic ground and first excited state. The effect of the environment (nuclear movement, protein scaffold) is modeled by frequency-independent (white noise) Gaussian fluctuations of the site energies. The fluctuations are temporarily (Markovian) and spatially uncorrelated. While the spatial correlations could be implemented, but seem to be not important, the main drawback is the fact that the framework is not suitable to describe non-Markovian effects. Under these assumptions an exact Liouville-von-Neumann equation was obtained (Haken-Strobl-Reineker), where the bath leads to pure dephasing with one free parameter (in principle one for each site), the dephasing rate γ. We discussed the applicability of the model by reviewing an alternative microscopic derivation and compared the dephasing rates with those obtained from experiments. This comparison suggests that we should be careful with the interpretation of the results obtained with dephasing rates beyond $10\,\mathrm{ps}$. Moreover, we completed the model by introducing additional terms on the level of the Liouville-von-Neumann equation that allow for local excitation trapping in order to include the irreversible transfer to a reaction center, and local dissipation of excitation energy.

4 Efficiency

The quantity that is most important for those green sulfur bacteria that live at a depth of 2,500 meters beneath the surface of the Pacific Ocean Beatty *et al.* (2005) is the efficiency of the excitation transport process. In this inhospitable environment, where no sunlight reaches, they have to live of the low probability to absorb a thermal photon.

In this Chapter, we first give a definition of the transport efficiency. With this quantity at hand, we proceed to discuss the interplay of the timescales of dephasing and trapping in the FMO model from the viewpoint of a disordered fully connected open quantum network and compare the results with a model where the site energies are set to zero. This represents a network without disorder in the site energies. Thereafter, we investigate the influence of different initial conditions that are motivated by the structure and orientation of the complex. We relax the typical assumption that the transfer to the reaction center takes place at site 3 and study also the effects of the trapping process at site 4, which is also located close to the reaction center.

4.1 Definition

The probability that an excitation is transferred from site i to the reaction center within the time interval $[t, t + dt]$ is given by

$$dp = 2\kappa_i \langle i| \rho |i\rangle \, dt, \tag{4.1}$$

where the trapping rates κ_i were introduced in Eqs. (3.11) and (3.12). This leads to a definition of the efficiency as the integrated probability of trapping up to a certain time τ which is characterized by the timescale of the transport process,

$$\eta = 2 \sum_i \kappa_i \int_0^\tau dt \, \langle i | \, \rho(t) \, | i \rangle \, . \tag{4.2}$$

This is nothing else than the population of the reaction center at time τ. If we consider purely coherent transfer* for the moment, we can estimate the timescale on which the transport process should be finished by looking at the inverse of the smallest off-diagonal elements in the Hamiltonian. These are on the order of $1\,\mathrm{cm}^{-1}$ corresponding to transfer time of approximately $5\,\mathrm{ps}$. Therefore, we fix $\tau = 5\,\mathrm{ps}$ in the following.

4.2 Role of Trapping and Initial Superposition

The discussion about the excitation transfer in the FMO complex converged to the role of the environment. It has been pointed out that pure coherent transfer can not explain the high transfer efficiency Hoyer *et al.* (2010); Mohseni *et al.* (2008b); Chin *et al.* (2010). However, we will see that this is not always true. Dephasing-assisted transport, as Chin *et al.* (2010) termed it, has been identifyed as a general feature of ordered and disordered networks, and it is robust against non-Markovianity. Other studies which focused on the effects of non-Markovianity or of spatial correlations of the environmental fluctuations are strongly model-dependent, and the conclusions are not clear and often conflicting. For progress in this direction, experiments that are capable of distinguishing between bath models are needed.

Besides that, the interplay of dephasing and trapping was investigated numerically in Gaab and Bardeen (2004) for finite linear systems and rings, and more recently in Cao (2009) also analytically for systems consisting of two to four sites. We briefly review the main results of this paper:

1. In a linear arrangement of three sites without detuning (equal site energies) the minimal transfer time is obtained for vanishing dephasing.

2. In the presence of detuning, the line-broadening effect of dephasing leads to a minimization of the transfer time.

*Besides the trapping process.

3. In topologies with closed loops, phases in the couplings lead to a modulation of the transfer time because of pathway interference.

The last point can already be seen as a motivation to study the influence of a phase in initial superpositions. Besides that, the geometrical aspect that sites 1 and 6 are both oriented towards the antenna as well as the proximity and strong coupling of sites 1 and 2 fuel the following investigations. In general, we note that until now, there was no emphasis on the connection between dephasing, the location of trapping and the impact of non-local superpositions in the initial states. In the following, we will close this gap. First, we will show that under preservation of the usual assumption of trapping at site 3, it is possible to achieve high efficiency by choosing a proper superposition of an initial excitation at sites 1 and 2. We will explain this observation with a consideration of Chin *et al.* (2010) and Plenio and Huelga (2008). After that, we will switch on trapping at site 4. We will see that there is a regime of trapping rates that allow efficient transfer with *and* without dephasing which is even quite unaffected by the choice of the initial condition. Finally, we will investigate the scenario where trapping at site 3 is switched off. Here, we find that an initial excitation almost localized at site 6 leads to efficient transfer for dephasing rates up to $100\,\mathrm{ps}^{-1}$, and that trapping at site 4 is in general beneficial.

4.2.1 Trapping at Site Three

In the case of the FMO complex, the usual assumption is trapping at site 3 with various rates ranging from $0.25\,\mathrm{ps}^{-1}$ Adolphs and Renger (2006) over $1\,\mathrm{ps}^{-1}$ Mohseni *et al.* (2008b) up to $6\,\mathrm{ps}^{-1}$ Chin *et al.* (2010). Besides that, only Kreisbeck *et al.* (2011) considered trapping at site 3 and 4 with rates of $2.5\,\mathrm{ps}^{-1}$, but didn't discuss it.

Figs. 4.1(a) and 4.1(b) show the efficiency as a function of dephasing and the trapping rate at site 3. In Fig. 4.1(b), the site energies are set to zero, which represents a setting without detuning. Both figures show the same characteristic behavior. As a function of the trapping rate, the efficiency starts to rise, when the trapping rate is around $1\,\mathrm{ps}^{-1}$. Surprising at first sight, if the trapping rate reaches the threshold on the order of $100\,\mathrm{ps}^{-1}$, the efficiency suddenly drops again. This is due to the decoupling of the trapping site from the rest of the system, as explained by Barvik and Herman (1992). The strong local dephasing at the trapping site decreases the probability to find an excitation at there, and hence the trapping process becomes inefficient. The drop with high dephasing stems from the *Quantum Zeno* effect (cf. Appendix A.3). We have already seen that the regime of

dephasing rates beyond $10\,\mathrm{ps}^{-1}$ should be treated with caution (Sec. 3.2.1). For strong environmental interactions the dynamics should be describable by incoherent rate equations where the rates are calculated by Fermi's golden rule, as done in Förster's theory. This theory which can be derived by classical arguments will not lead to the quantum zeno limit. Therefore, we conclude that strong environmental interaction in the FMO complex cannot be modeled solely by stochastic fluctuations of the site energies.

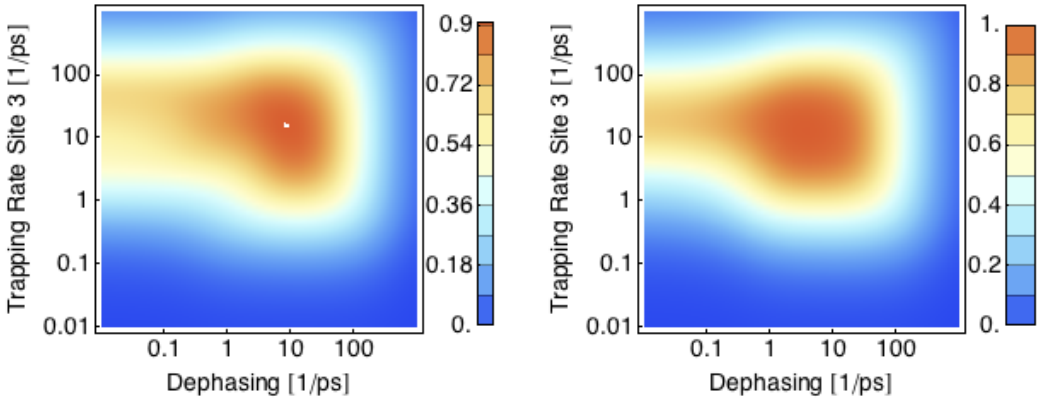

(a) Full FMO Hamiltonian.

(b) Here, site energies are set to zero.

Figure 4.1: Efficiency as a function of dephasing and the rate of trapping at site 3. The initial state is an excitation at site 1. The white dot in the left figure indicates efficiency above 90 %.

We proceed with discussing the regions of high efficiency. We see that for the trapping rates typically used, high efficiency can only be achieved for dephasing rates on the order of $10\,\mathrm{ps}^{-1}$. Without detuning, even rates on the order of $1\,\mathrm{ps}^{-1}$ are sufficient. But remarkably, also in this case optimal efficiency is obtained for non-zero dephasing. This is in contrast to the observations made in a linear chain without detuning we mentioned in the enumeration above (4.2). In the full system with disordered site energies, dephasing can enhance transport due to line broadening. In Sec. 3.2.1, we saw that the effect of pure dephasing on the density matrix level came from stochastic fluctuations of the site energies on the level of the Hamiltonian. Therefore, strong dephasing is equivalent to large fluctuations of the site energies, which is able to shift the energy levels in resonance. If there is no detuning, the site energies are already in resonance and line broadening can therefore not be the explanation. But we can think of destructive interference of transport pathways that hinders transport in the coherent case. The fact that interference may play an important role in the transfer process motivates the study of the role of the initial condition, especially the phase dependence of initial non-local superpositions, since this is a pure quantum effect.

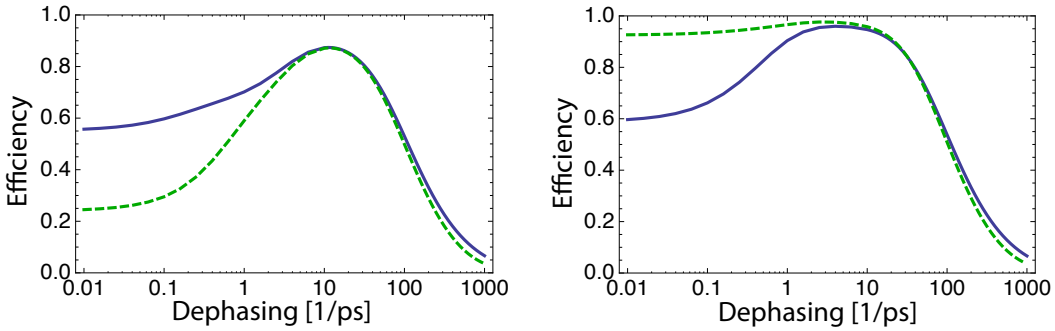

(a) Complete FMO Hamiltonian.

(b) Site energies are set to zero.

Figure 4.2: Efficiency as a function of dephasing and trapping at site 3 with a rate of $5\,\mathrm{ps}^{-1}$. The blue lines correspond to an initial excitation at site 1, while the green, dashed lines denote an initial excitation at site 6.

Influence of Initial Condition

Because of the alignment of the FMO complex respective to the light harvesting antenna, the typical assumption is an initial excitation at site 1 *or* at site 6 (cf. Sec. 2.1 and especially Fig. 2.2). In the following, we fix the trapping rate at site 3 to be $5\,\mathrm{ps}^{-1}$. This is comparable to the trapping rates other authors use and also allows for high efficiencies. Before we concentrate on superpositions, we start with the common initial conditions for comparison.

The Figs. 4.2 can be seen as a cut through Figs. like 4.1 for a fixed trapping rate. In Fig. 4.2(a), we note that for low dephasing rates, the efficiency for an initial excitation at site 1 is more than double the efficiency for an initial excitation at site 6. This is because there is a direct transfer path from site 1 over the strong coupled site 2 to site 3. In contrast, the transfer from site 6 offers more opportunities for destructive interference (c.f. Fig 4.3) and even more importantly, the detuning between the sites involved in this transport pathway is much more pronounced. For a dephasing rate around $10\,\mathrm{ps}^{-1}$, the difference between the two initial conditions vanishes, but still almost 20% of the excitation is stuck in a slow transfer channel. If we switch off the detuning (cf. Fig. 4.2(b)), the efficiency for an initial excitation at site 6 increases dramatically in the low dephasing regime. This underpins the statement that the detuning impedes the excitation transfer from site 6 and that the line broadening effect of dephasing is crucial. Especially since site 6 and site 5, which are part of the fast transport channel have the highest site energies. In contrast, the transport from site 1 is hardly affected, at least in the limit of low dephasing. Moreover, the maximum efficiency reaches almost unity and for both initial states the maximum

efficiency is obtained for non-zero dephasing.

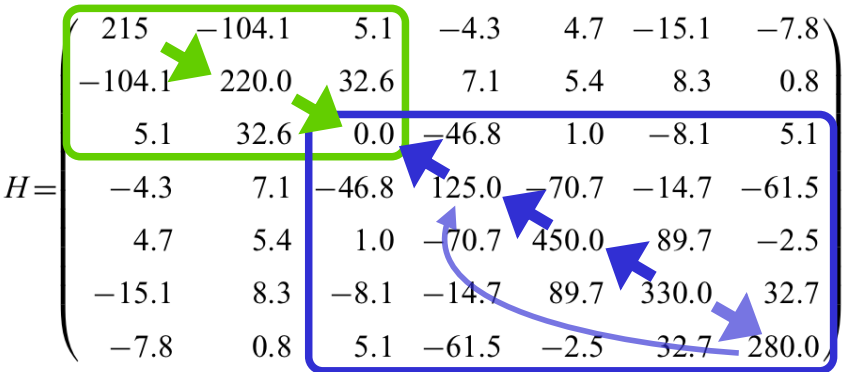

Figure 4.3: The FMO Hamiltonian with main transfer paths given by the magnitude of the couplings.

It is natural to proceed with investigating the superposition of $|1\rangle$ and $|6\rangle$, because they are both located close to the antenna (cf. Sec. 2.1) and therefore both have a finite probability to get excited by the antenna.

We assume equal probabilities to find an excitation at site 1 and site 6 and concentrate solely on the effect of the phase angle ϕ. The initial state is then

$$|\psi\rangle_{init} = \frac{1}{\sqrt{2}}(|1\rangle + \mathrm{e}^{-i\phi}\,|6\rangle\,. \tag{4.3}$$

As can be seen in Fig. 4.4, the phase dependency is insignificant. The behavior is similar to a classical mixture. Only for very low dephasing there is a slight modulation of the efficiency (below 10%). This is not very surprising. If we take into account only the strongest couplings (above $30\,\mathrm{cm}^{-1}$), the two pathways are just connected through site 3 (cf. Fig. 4.5). Since site 3 is the trapping site, it is exposed to local dephasing due to the trapping process, and the interference is destroyed.

A scenario probable under laser excitation, would be a superposition between site 1 and site 2. These are the sites which exhibit the largest coupling within the complex ($v_{1,2}$ = $-104.1\,\mathrm{cm}^{-1}$ in comparison to $v_{1,6}$ = $-15.1\,\mathrm{cm}^{-1}$). Due to this strong coupling and the proximity of the two sites, an excitation will immediately be delocalized. If the duration of the laser pulse (e.g. 38 fs in Hayes and Engel (2011)) is comparable to the timescale of the coherent oscillations between the two sites (about 50 fs), it is reasonable to expect a superposition. In addition, excitation transport from site 8 (cf. Fig. 1 of Hoyer *et al.* (2011)) could in principle also create such a state. Thus, we will now discuss the

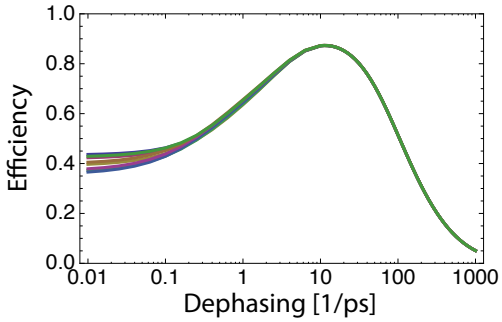

Figure 4.4: Efficiency as a function of dephasing for various initial phases between $|1\rangle$ and $|6\rangle$.

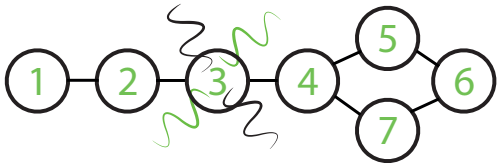

Figure 4.5: Illustration of the topology of the FMO network when only the strongest couplings are considered. The local dephasing at site 3 due to the trapping process is indicated by the wiggly lines.

implications of an initial excitation of the form

$$|\psi_{init}\rangle = \cos(\theta)\,|1\rangle + \mathrm{e}^{-i\phi}\sin(\theta)\,|2\rangle\,. \tag{4.4}$$

At first sight, there seems to be no difference in Figs. 4.6(a) and 4.6(b), but the scaling is very distinct. While in Fig. 4.6(a), the brightest (darkest) spots represent an efficiency of about 98% (9%), the maximum (minimum) in Fig. 4.6(b) is at 77% (63%). This allows two conclusions. Firstly, without dephasing, there is an extraordinary dependency of the efficiency on the superposition angles. Secondly, if the initial excitation is chosen optimally, dephasing will reduce the efficiency. In contrast, the superpositions leading to low efficiency for zero dephasing will be enhanced by the dephasing process.

We label the marginal initial states as $|best\rangle$ and $|worst\rangle$ and recognize that they are given by

$$|best\rangle = \frac{1}{\sqrt{2}}(|1\rangle + |2\rangle) \quad \text{and} \quad |worst\rangle = \frac{1}{\sqrt{2}}(|1\rangle - |2\rangle). \tag{4.5}$$

Forming the scalar product $\langle best|\ worst\rangle$, we see that these states are orthogonal and coincide with the $|+\rangle$ and $|-\rangle$ states in Chin *et al.* (2010). In this paper, *Chin* uses these states to change to a hybrid basis and explains the observed effect by arguing that $|best\rangle$ is

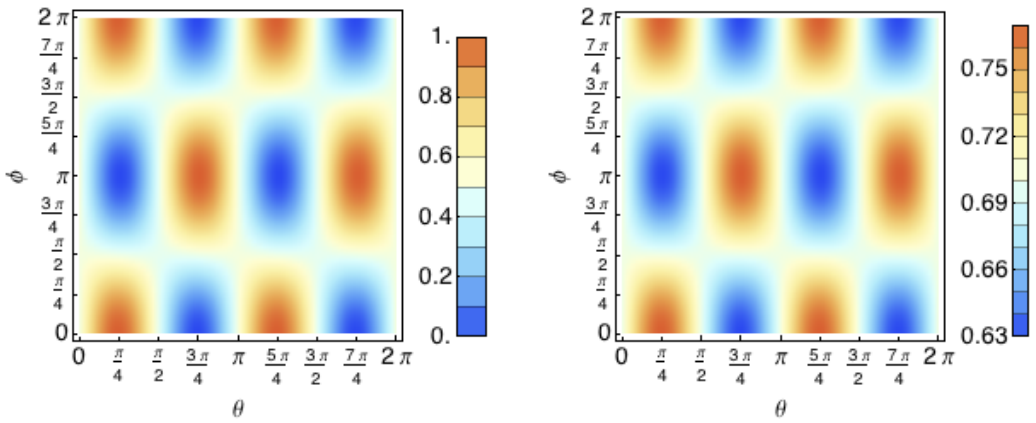

(a) Dephasing is zero. The brightest spot corresponds to an efficiency of 98%, the darkest to 9%.

(b) Dephasing is 1 ps^{-1}. The brightest spot corresponds to an efficiency of 77%, the darkest to 63%.

Figure 4.6: Efficiency for initial superpositions of site 1 and site 2. Trapping at site 3 with rate $5\,\mathrm{ps}^{-1}$.

shifted towards $|3\rangle$, allowing for fast near-resonance transfer, while $|worst\rangle$ is shifted to resonance with $|6\rangle$, which leads coherent oscillations between these two sites. Activating dephasing, two things are happening if we start in $|best\rangle$. Dephasing jiggles the site energies and impedes the resonant transfer to site 3, and also destroys the superposition. This can be seen as opening an incoherent transfer channel to $|worst\rangle$. Starting in $|worst\rangle$ the latter effect leads to the enhancement of efficiency seen in Figs. 4.6(b) and 4.7. Now, we can easily explain the blue line in Fig. 4.2(a). The state $|1\rangle$ can be seen as a superposition of the states $|best\rangle$ and $|worst\rangle$, where both states are equally populated. If we add up the efficiencies of $|best\rangle$ and $|worst\rangle$, as seen in Fig. 4.7, and normalize the resulting efficiency by dividing by two, we end up with the blue line in Fig. 4.2(a). We can also give an explanation for the rather low maximum efficiency around 80% in this plot. Since $|worst\rangle$ is shifted towards $|6\rangle$, we can think of a fraction of the excitation that takes the route through site 6 and hence suffers from a low probability to be at the trapping site in time.

It is interesting to look not only at the integrated trapping probability, but also at the evolution of the reaction center population. Fig. 4.8 shows the reaction center (RC) population for the two marginal initial states and different dephasing rates. In Fig. 4.8(a), we observe a steep rise in the RC population between 0.5 and 1 ps in the limit of low dephasing. The crossing of the black and red line is due to the minimum seen in 4.7. Comparing Figs. 4.8(a) and 4.8(b) (especially the insets), we see that the spreading with

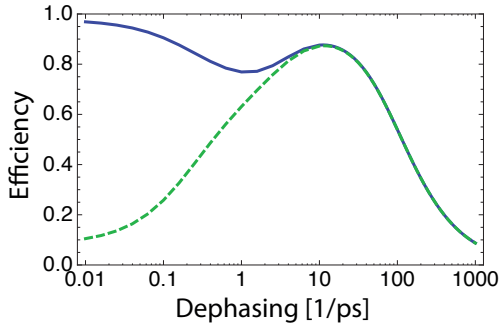

Figure 4.7: Efficiency as a function of dephasing. The blue line represents starting in $|best\rangle$, the green, dashed line in $|worst\rangle$. Trapping at site 3 with rate $5\,\mathrm{ps}^{-1}$.

different dephasing rates begins an order of magnitude earlier in the case of $|worst\rangle$ being the initial state and is more pronounced. For longer times, the latter was already observed in Fig. 4.7.

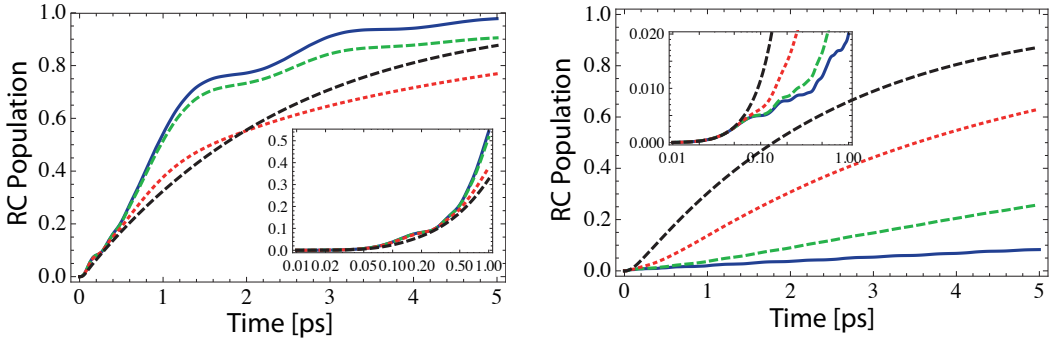

(a) Initial state is $|best\rangle$.

(b) Initial state is $|worst\rangle$.

Figure 4.8: Reaction center population as a function of time for different dephasing rates (blue solid: 0, green dashed : 0.1, red dotted: 1, black dashed: $10\,\mathrm{ps}^{-1}$). Trapping at site 3 with rate $5\,\mathrm{ps}^{-1}$.

Conclusion

In summary, we note that there is a regime in the parameter space spanned by the dephasing rate and the trapping rate that allows highly efficient transfer. Remarkably, this regime begins usually for non-zero dephasing and it seems that the trapping rates should be on the order of the coupling elements in the Hamiltonian. While this has already been known for disordered networks, we have seen that it can also be true for networks without detunings. Further, we found that efficient *coherent* transport can also be achieved by

choosing an optimal initial superposition. In this case, adding dephasing hinders transport. Therefore, if the protein environment is able to protect coherence and superpositions, the transport process could benefit from a proper superposition in the initial excitation of the complex.

4.2.2 Trapping at Site Four

In the next step, we introduce an additional trapping process at site 4. In Fig. 4.9, the efficiency as a function of the trapping at site 3 and site 4 is shown. It is important to note that there is no additional dephasing involved. Nevertheless, there is a broad regime of near-unit efficiency. By comparing both plots, it is striking that the functional role of the two trapping sites seems to be interchanged. This can be understood by looking at the main excitation transfer pathways again (c.f. Fig. 4.3). Site 1 is more directly coupled to site 3, and site 6 more to site 4. Another outstanding feature is captured in Fig. 4.9(b). As the trapping rate at site 4 reaches a threshold of about $5\,\mathrm{ps}^{-1}$, the efficiency becomes almost independent of the trapping rates at site 3 and site 4 for a wide range. For this reason, we will now investigate the situation where site 3 is decoupled from the RC and site 4 acts as the only trap with rate $5\,\mathrm{ps}^{-1}$.

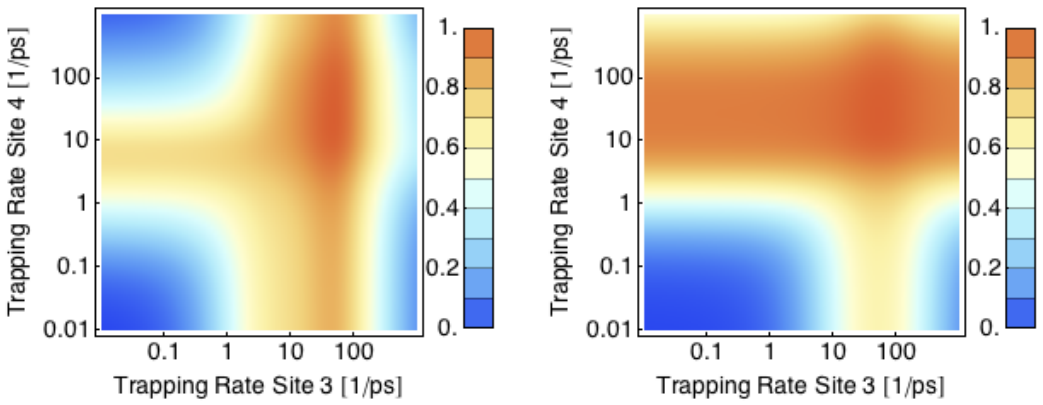

(a) Initial excitation at site 1.

(b) Initial excitation at site 6.

Figure 4.9: Efficiency as a function of trapping rates at site 3 and site 4. The dephasing is set to be zero.

Influence of Initial Condition

Fig. 4.9 gives reason to expect a strong dependence at least on the angle θ of the superposition

$$|\psi_{init}\rangle = \cos(\theta)\,|1\rangle + \sin(\theta)\,\mathrm{e}^{-i\phi}\,|6\rangle\,. \tag{4.6}$$

More interesting is the question if there is also a strong dependence on the phase angle ϕ. Looking at Fig. 4.10(a), we can affirm this question. If we fix $\theta = \frac{\pi}{4}$ and scan over ϕ, the modulation of the efficiency is significant. Similar to the case of a superposition of $|1\rangle$ and $|2\rangle$ with trapping at site 3, the symmetric ($\phi = 0$) superposition is efficient while the antisymmetric ($\phi = \pi$) is not. Furthermore, we recognize that it is beneficial when the excitation is mainly localized at site 6 ($\theta \approx \frac{n\pi}{2}$) and unfavorable when it is mainly localized at site 1 ($\theta \approx n\pi$). This, of course, agrees with the intuitive picture of the main transport paths we discussed repeatedly. But surprisingly, the optimal (pessimal) transport is not obtained for $\theta = \frac{n\pi}{2}$ ($\theta = n\pi$), and we can transfer some population to site 1 (by changing θ) without affecting the efficiency much if we adjust the phase angle ϕ accordingly. Now, we activate dephasing. In Fig. 4.10(b), we see the efficiency of a superposition leading to optimal and pessimal transport for zero dephasing ($\theta_{opt} = \frac{17\pi}{50}$, $\phi_{opt} = 0$ and $\theta_{pes} = \frac{21\pi}{25}$, $\phi_{pes} = 0$) as a function of dephasing. We will refer to those states as $|opt\rangle$ and $|pes\rangle$ in what follows. Remarkably, the efficiency in the optimal case is almost constant in the range of interest (up to the order of $10\,\mathrm{ps}^{-1}$), and on a high level (around 90%). This is a desirable situation which could be interesting for engineering artificial "quantum wires". There it should be possible to control the initial condition and the demand is robustness against noise. Here, we have shown that this is indeed possible. In addition, we can observe a complete new feature. In all other plots, the decay of the efficiencies for high dephasing coincides for the investigated initial conditions. But here, the blue and the green line deviate significantly which shows that a modulation of the efficiency in the high dephasing regime by changing the initial superposition is possible. Although we must not forget that the model is not appropriate for dephasing rates beyond $10\,\mathrm{ps}^{-1}$.

Since we have seen that a proper superposition of $|1\rangle$ and $|2\rangle$ can lead to a rich enhancement of efficiency in the case of trapping at site 3, we want to explore this scenario also for trapping at site 4.

As can be seen in Fig. 4.11, the situation is quite similar. The superpositions that lead to the marginal efficiencies are exactly the same. But the effect is not as pronounced as in

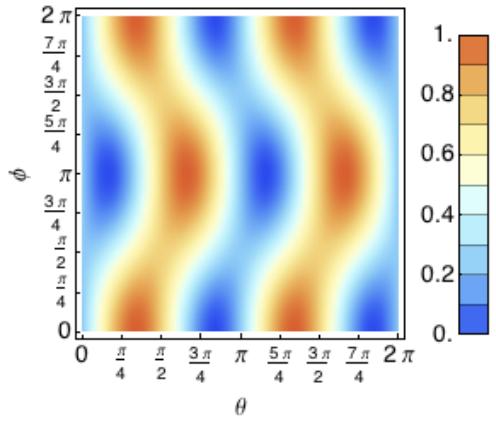

(a) Efficiency as a function of the initial excitation defined in Eq. 4.6. Dephasing is zero.

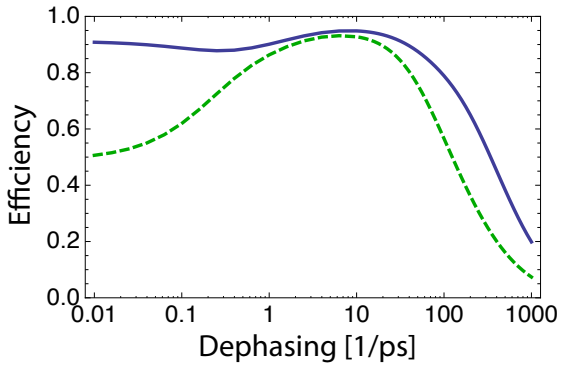

(b) Efficiency as a function of dephasing. The blue line represents the initial condition leading to maximum efficiency for zero dephasing ($|opt\rangle$), the green, dashed line leads to minimal efficiency ($|pes\rangle$).

Figure 4.10: Efficiency for trapping at site 4 with rate $5\,\mathrm{ps}^{-1}$.

the case of trapping at site 3. The maximum difference is only 63%, in comparison to the 89% before (Fig. 4.6(a)).

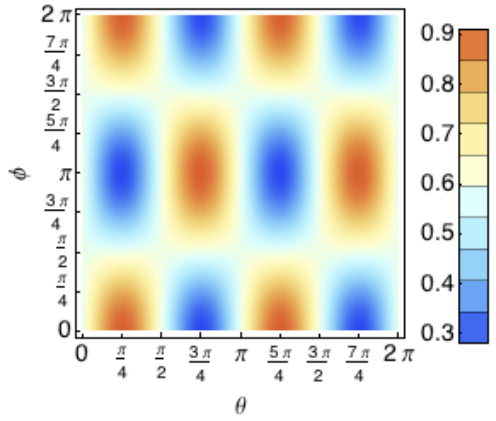

(a) Efficiency for initial superpositions of $|1\rangle$ and $|2\rangle$. No dephasing.

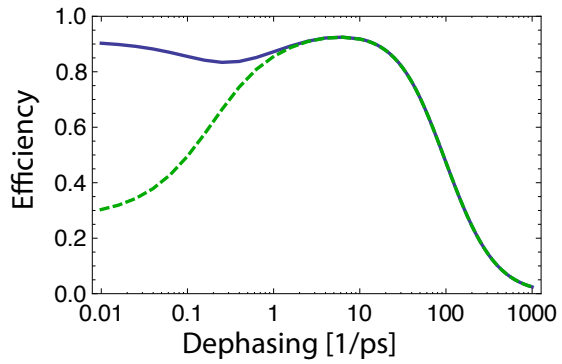

(b) Efficiency as a function of dephasing. The blue line represents starting in $|best\rangle$, the green, dashed line in $|worst\rangle$.

Figure 4.11: Efficiency for trapping at site 4 with rate $5\,\mathrm{ps}^{-1}$. Dephasing is set to zero.

All in all, it seems that trapping at site 4 would be favorable. Of course, as we have seen in the beginning of this Section, additional trapping at site 3 will not change much, but can only be an enhancement. But what is it that distinguishes site 4? We try to answer this question by looking at a measure of the connectivity of a site. We define the connectivity

of the site j by

$$\zeta_i = \sum_{i \neq j} |v_{ij}|, \tag{4.7}$$

where v_{ij} denotes the coupling between site i and site j. We see that site 4 ($\zeta_4 = 330.1\,\mathrm{cm}^{-1}$) is much better connected than site 3 ($\zeta_3 = 98.7\,\mathrm{cm}^{-1}$). Moreover, site 4 has the highest connectivity of the complete network.

4.3 Conclusion

At this point we close the discussion concerning the efficiency of the transport process. While it was known that dephasing can enhance transport, we have shown here that a superposition of an excitation at two entry sites can lead to high efficiency even in the case of completely coherent transport. Moreover, the efficiency is quite robust against dephasing. This effect can even be strengthened by allowing for trapping at site 4. We made this plausible by computing the connectivity of the sites.

5 Entanglement and Correlations

Since there was evidence of quantum effects in the form of quantum beats in the experiments, and we saw in the last chapter that coherent superpositions can modulate the efficiency, it is natural to ask for the role of quantum correlations. The well-established incarnation of quantum correlations is entanglement. It is known that entangled systems can be in advantage to perform certain tasks, and entanglement was identified as a resource. More recently, it was recognized that also non-entangled states can exhibit quantum correlations. Thus, we will introduce one of those measures of quantum correlations that reach beyond entanglement. This measure is called *quantum discord* Ollivier and Zurek (2001) and has attracted a lot of interest in the past few years.

Interestingly, we will prove that in the zero- and single-excitation subspaces quantum discord and relative entropy of entanglement coincide, at least under the assumption of vanishing coherences between those two subspaces, as given in our model. Since Sarovar *et al.* (2011) showed that coherence in the site basis is equivalent to entanglement, we will be able to conclude that all effects based on quantum correlations are hidden in the persistence of coherence in the site basis.

In the second part of this chapter, we look at the time evolution of quantum and classical correlations between the sites that are excited initially and the trapping site, as well as at their response to dephasing. Thereby, we concentrate essentially on the initial conditions we found in the last chapter. Finally, in the last section, we investigate the dynamics of quantum correlations of coherent and non-coherent initial states with higher excitations.

5.1 Definitions

In this section, we define entanglement and the entanglement measures we will use afterwards. After that, we will define quantum discord and give an example of a non-entangled state that exhibits non-zero quantum discord. Therefore, this section is rather technical.

5.1.1 Entanglement

Since we are dealing with an open quantum system, our system will usually be in a mixed state. Therefore, we consider the case of bipartite entanglement for mixed states.

Imagine, to stay within our molecular framework, a dimer. The system consists of two sites which are spatially separated. We denote one site as A and the other as B. The density matrix of the whole dimer is ρ. We call ρ a *product state*, if we can write

$$\rho = \rho^A \otimes \rho^B. \tag{5.1}$$

Further, we say the state is *separable*, if there exist $p_i \geq 0$, with $\sum_i p_i = 1$, and product states $\rho_i^A \otimes \rho_i^B$ such that

$$\rho = \sum_i p_i \rho_i^A \otimes \rho_i^B. \tag{5.2}$$

If we can not write the state in this form, it is called *entangled*.

While the definition is quite easy, there is no general algorithm or criterium to find out if a given state is separable*, except for some classes of states. But there exist at least some criteria that imply separability or entanglement. Moreover, there is even the possibility to quantify (although different measures yield different results) the amount of entanglement.

In the following, we introduce two of them, the relative entropy of entanglement and the logarithmic negativity, and use them to quantify entanglement present in our model of the excitation transport in the FMO complex.

*For a general two-qubit system there is such a criterium, but not for a system consisting of more qubits or objects of higher dimensionality.

Relative Entropy of Entanglement

The *relative entropy of entanglement* Vedral *et al.* (1997) belongs to the class of distance measures Gühne and Tóth (2009) and measures, in its basic definition, the global entanglement of a state. Thus, it is defined as the minimal distance of a state ρ to the next separable state σ^*,

$$E_R(\rho) = S(\rho \parallel \sigma^*) = \inf_{\sigma \in \mathcal{S}} S(\rho \parallel \sigma). \tag{5.3}$$

The quantity $S(\rho \parallel \sigma) = \mathrm{tr}[\rho \log(\rho) - \rho \log(\sigma)]$ is the relative entropy, and is not a true metric, since it is not symmetric under the interchange of ρ and σ.

Besides this global measure, we can also define a bipartite version,

$$E_R(\rho) = \inf_{\sigma^{AB} \in \mathcal{S}} S(\rho \parallel \sigma^{AB}). \tag{5.4}$$

Logarithmic Negativity

The *logarithmic negativity* Plenio (2005); Plenio and Virmani (2007) is an easy-to-compute entanglement measure for bipartite systems. It originates from the PPT (positive partial transpose) criterium of separability which states that the positivity of the partial transpose of a state is a necessary condition for separability. The partial transposition of a bipartite state represented by the density matrix $\rho^{AB} = \sum \rho_{ij,kl} \left|i\right\rangle \left\langle j\right|^A \otimes \left|k\right\rangle \left\langle l\right|^B$ with respect to subsystem B is defined as

$$\rho^{T_B} = \sum_{i,j,k,l} \rho_{ij,kl} \left|i\right\rangle \left\langle j\right|^A \otimes \left|l\right\rangle \left\langle k\right|^B. \tag{5.5}$$

To quantify the negativity in the spectrum of the partial transpose, one can define the negativity

$$N(\rho) = \frac{\|\rho^{T_B}\|_1 - 1}{2}, \tag{5.6}$$

where $\|X\|_1 := \sqrt{X^\dagger X}$ is the trace norm. The negativity is a convex entanglement monotone, but is not additive. We will use a related quantity that is additive but not convex, the *logarithmic negativity*

$$E_N(\rho) = \log_2 \|\rho^{T_B}\|_1 \tag{5.7}$$

The use of the *logarithmic negativity* will be in quantification of entanglement beyond single excitations, because in this case there is no known formula to calculate the relative

entropy of entanglement without an expensive optimization procedure. If we restricted ourselves to the case of the bipartite entanglement between two sites, e.g. one entry and one trapping site, we could also use the *concurrence* or the related *entanglement of formation* to quantify entanglement efficiency because of the famous analytical formula found by Wootters (1998).

5.1.2 Quantum Discord

In classical information theory there exist two equivalent formulas for the mutual information to quantify the strength of all correlations present in a bipartite system. The difference of the quantum versions of these leads to a measure of the quantum excess correlations called *quantum discord* Ollivier and Zurek (2001).

We start here by introducing the *mutual information* in the context of classical information theory. There, it quantifies the correlation between two random variables X and Y, and is defined by

$$J(X:Y) = H(X) - H(X|Y), \tag{5.8}$$

where H is the classical Shannon entropy and $H(X|Y) = \sum_y p_{Y=y} H(X|Y=y)$ is the conditional entropy of X given Y. Hence, the mutual information measures the average decrease of entropy on X when Y is found. By applying Bayes rule Koch (2000)

$$p_{X|Y=y} = \frac{p_{X,Y=y}}{p_{Y=y}} \tag{5.9}$$

one can show that $H(X|Y) = H(X,Y) - H(Y)$ which leads directly to another classically equivalent expression for the mutual information:

$$I(X:Y) = H(X) + H(Y) - H(X,Y) \tag{5.10}$$

Now, we proceed by defining I and J for quantum systems. The original application was for bipartite systems consisting of the actual physical system and a measurement apparatus. In the following we are not so restrictive and define the quantities for arbitrary bipartite quantum systems. In the case of I it is no problem to generalize to the quantum case. All we have to do is to replace the classical Shannon entropy H by the von-Neumann entropy S,

$$I(\rho_{AB}) = S(\rho^A) + S(\rho^B) - S(\rho^{AB}). \tag{5.11}$$

In the case of J, the quantum version is more involved. This is because the conditional entropy $H(A|B)$ requires us to specify the state of A given the state of B which implies a measurement on subsystem B. We restrict ourselves to perfect measurements, and therefore consider a complete set of projectors $\{\Pi_j^B\}$, such that $\sum_j \Pi_j^B = \mathbb{1}$. The state of the subsystem A after this measurement is

$$\rho^{A|\Pi_j^B} = \mathrm{tr}_B(\Pi_j^B \rho^{AB} \Pi_j^B) / \mathrm{tr}(\Pi_j^B \rho^{AB}), \tag{5.12}$$

with probability $p_j = \mathrm{tr}(\Pi_j^B \rho^{AB})$. Knowing this, we can write down the conditional entropy in the quantum case

$$S(\rho^A|\{\Pi_j^B\}) = \sum_j p_j S(\rho^{A|\Pi_j^B}) \tag{5.13}$$

and the quantum analogue of J (Eq. 5.8 is

$$J(\rho_{AB})_{\{\Pi_j^B\}} = S(\rho^A) - S(\rho^{A|\{\Pi_j^B\}}). \tag{5.14}$$

The *quantum discord* then is defined as the minimum of the difference between I and J:

$$D(\rho^{AB}) = \min_{\{\Pi_j^B\}}[I(\rho^{AB}) - J(\rho^{AB})_{\{\Pi_j^B\}}] \tag{5.15}$$

$$= S(\rho^B) - S(\rho^{AB}) + \min_{\{\Pi_j^B\}} S(\rho^A|\{\Pi_j^B\}). \tag{5.16}$$

We can give a general intuition in the case that ρ^{AB} is a pure state. In this instance, the last two terms vanish. The second one does, because the von-Neumann entropy is zero for pure states, and the third one vanishes for the same reason due to the purity of each $\rho^{A|\Pi_j^B}$. Since $S(\rho^B) = S(\rho^A)$ for a pure state ρ^{AB}, $S(\rho^B)$ is an unique identifier for entanglement and thus, quantum discord reduces to entanglement.

In addition, the nature of quantum discord as a measure of quantum correlations is also revealed by the fact that Henderson and Vedral (2001) identified J as a measure of classical correlations independent of Ollivier and Zurek (2001). Then, of course, the difference between the total correlations and the classical correlations is a reasonable measure of the quantum correlations.

The minimization in Eq. (5.15) seeks for the measurement on subsystem B that least disturbs the total quantum state and thus allows to obtain as much information as possible

from the subsystem A Auyuanet and Davidovich (2010). In fact it has been shown that

$$D(\rho^{AB})_{\{\Pi_j^B\}} = 0 \quad \Leftrightarrow \quad \rho^{AB} = \sum_j \Pi_j^B \rho^{AB} \Pi_j^B, \tag{5.17}$$

which says that quantum discord vanishes if and only if ρ^{AB} is a quantum-classical state. Like relative entropy of entanglement, quantum discord is not a symmetric measure.

There is also a global version of quantum discord. The very appealing notion was given by Modi *et al.* (2010) to present a *'Unified View of Quantum and Classical Correlations'*. Therein, the quantum discord of a state ρ is given by the minimal distance, again measured by the relative entropy, to the next *classical* state χ^*,

$$D(\rho) = \min_{\chi \in \mathcal{C}} S(\rho \parallel \chi). \tag{5.18}$$

The set of classical states $\mathcal{C}$ is defined as the set containing mixtures of *locally distinguishable states*

$$\chi = \sum_{k_i} p_{k_1 \ldots k_n} |k_1 \ldots k_n\rangle \langle k_1 \ldots k_n| = \sum_{\vec{k}} p_{\vec{k}} |\vec{k}\rangle\langle\vec{k}|, \tag{5.19}$$

where the $p_{k_1 \ldots k_n} \geq 0$ and $\sum_{k_i} p_{k_1 \ldots k_n} = 1$, and the *local states* $|k_i\rangle$ span an orthonormal basis. The emphasis here is really on the local states. While we can diagonalize every density matrix since it is Hermitian, a state is only classical if the density matrix is diagonal in a local basis. Considering our model system, the basis that diagonalizes the Hamiltonian is called the excitonic basis. If the density matrix is diagonal in this basis, the state is clearly non-local and therefore also non-classical. Instead, the site basis is local, and the states that are diagonal with respect to the site basis are classical. We will come back to this in the next section.

It has been shown that there are separable states exhibiting quantum correlations captured by the quantum discord (e.g. in Ollivier and Zurek (2001)). Therefore, quantum discord can be seen as a more general identifier of *quantumness* than entanglement. Recently, quantum discord could also be identified as a resource for quantum information tasks Datta and Shaji (2008) and operational interpretations were found Cavalcanti *et al.* (2011).

We will quickly reproduce the example of a separable state with non-zero quantum discord given in Ollivier and Zurek (2001) because we will use it again in the next section.

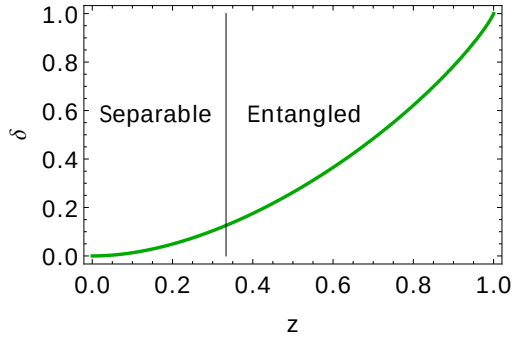

Figure 5.1: Quantum discord for two qubit Werner states.

We consider the Werner (1989) states,

$$|W\rangle = \frac{1-z}{4}\mathbb{1} + z\,|\psi\rangle\langle\psi| \quad \text{with} \quad |\psi\rangle = (|00\rangle + |11\rangle)/\sqrt{2}. \tag{5.20}$$

For $z = 1$, $|W\rangle$ is a maximally entangled Bell state, whereas for $z = 0$ the state is obviously separable. Concerning quantum discord one should note that $\mathbb{1}$ and $|\psi\rangle$ are invariant under local unitary rotations, and therefore discord does not depend on the choice of a measurement basis. In Fig. 5.1 it is shown that quantum discord is non-zero for $z \neq 0$, whereas entanglement sets in not before $z \geq 1/3$.

5.2 The Single-Excitation Subspace

Projecting the Werner state (5.20) into the zero- and single-excitation subspace, only the ground state part of the Bell state remains. The resulting (unnormalized) state,

$$\left|\tilde{W}\right\rangle_{01} = \frac{1-z}{4}\mathbb{1}_{01} + \frac{z}{2}\,|00\rangle\langle 00| \tag{5.21}$$

$$= \frac{1+z}{4}\,|00\rangle\langle 00| + \frac{1-z}{4}(|10\rangle\langle 10| + |01\rangle\langle 01|), \tag{5.22}$$

is separable, since every term is separable. By looking at Fig. 5.2, we see that quantum discord also vanishes.

We have seen that although a state can have non-zero quantum discord while being entangled in the full Hilbert space, a projection into the zero- and single-excitation subspace *can* lead to a coincidence of the two measures.

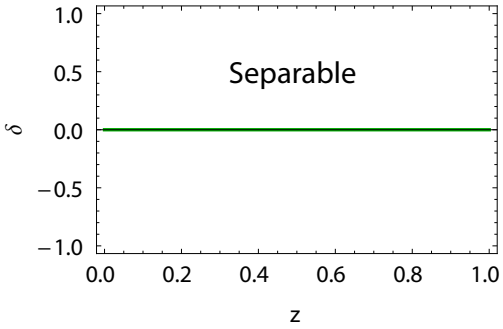

Figure 5.2: Quantum discord for two-qubit Werner states projected on zero- and single-excitation subspace.

5.2.1 Equivalence of Quantum Discord and Relative Entropy of Entanglement

In the case of our model system, the results of Brádler *et al.* (2010), as well as our own numerical studies, suggest that quantum discord coincides with the (bipartite) relative entropy of entanglement in the zero- and single-excitation subspaces. In the remainder of this section, we will support these findings by a more formal proof.

Global Versions

But first, we take a look at the global measures to get some intuition. Sarovar *et al.* (2010) showed that coherence in the site basis is necessary and sufficient for entanglement. More formally, they showed that

$$\rho \text{ entangled } \Leftrightarrow \langle i| \rho |j\rangle \neq 0 \text{ for some } i \neq j, \tag{5.23}$$

and moreover that the closest separable state is

$$\sigma^* = \sum_i |i\rangle \langle i| \rho |i\rangle \langle i| = \sum_i \rho_{ii} |i\rangle \langle i| . \tag{5.24}$$

Knowing the closest separable state, we recall the definition of a classical state (5.19), and note that the classical states also have the form

$$\chi = \sum_i p_i |i\rangle \langle i| . \tag{5.25}$$

Since the set of classical $\mathcal{C}$ and separable states $\mathcal{S}$ coincide in the single-excitation subspace, also the optimization will lead to the same result, $p_i = \rho_{ii}$. Also, Theorem 2 in Modi *et al.* (2010) states that the closest classical state to a state ρ is given by $\chi^* = \sum_{\vec{k}} |\vec{k}\rangle\langle\vec{k}|\rho|\vec{k}\rangle\langle\vec{k}|$, where $\{|\vec{k}\rangle\}$ forms the eigenbasis of χ^*. Identifying $\{|\vec{k}\rangle\}$ with $\{|i\rangle\}$ again leads to

$$\chi^* = \sum_i |i\rangle \langle i| \rho |i\rangle \langle i| = \sum_i \rho_{ii} |i\rangle \langle i| . \tag{5.26}$$

Therefore, $\sigma^* = \chi^*$, and (global) quantum discord and relative entropy of entanglement coincide in the single-excitation subspace.

Bipartite Versions

Next, we consider the bipartite versions. Since Eq. (5.15) for quantum discord involves an optimization of the measurement basis, the optimization parameters in principle grow with 2^{n_B}, where n_B denotes the number of sites in subsystem B. For this reason, we fix subsystem B to contain only one site. This restriction enables us to write projection operators as

$$\Pi_1^B = \mathbb{1}^A \otimes \begin{pmatrix} \cos^2(\theta) & \mathrm{e}^{-i\phi}\sin(\theta)\cos(\theta) \\ \mathrm{e}^{i\phi}\sin(\theta)\cos(\theta) & \sin^2(\theta) \end{pmatrix} \tag{5.27}$$

and

$$\Pi_2^B = \mathbb{1}^A \otimes \begin{pmatrix} \sin^2(\theta) & -\mathrm{e}^{-i\phi}\sin(\theta)\cos(\theta) \\ -\mathrm{e}^{i\phi}\sin(\theta)\cos(\theta) & \cos^2(\theta) \end{pmatrix}, \tag{5.28}$$

where we have chosen the computational basis of subsystem B to be

$$\begin{pmatrix} 1 \\ 0 \end{pmatrix} = |g\rangle \quad \text{and} \quad \begin{pmatrix} 0 \\ 1 \end{pmatrix} = |e\rangle . \tag{5.29}$$

To proceed, we note that the formula for quantum discord (5.15) can be written more explicitly as

$$D(\rho^{AB}) = S(\rho^B) - S(\rho^{AB}) + \min_{\{\Pi_j^B\}}[p_1 S(\rho^{A|\Pi_1^B}) + p_2 S(\rho^{A|\Pi_2^B})]. \tag{5.30}$$

Moreover, Brádler *et al.* (2010) derived a formula to calculate the bipartite relative entropy of entanglement

$$E_R(\rho^{AB}) = S(\Delta(\rho^{AB})) - S(\rho^{AB}), \tag{5.31}$$

where $\Delta(\rho^{AB}) = p_0 |0\rangle\langle 0| + \rho_e^A \otimes |g\rangle\langle g|^B + |g\rangle\langle g|^A \otimes \rho_e^B$ and p_0 is the population of the ground state and the subscript e denotes the projection into single-excitation subspace. This formula is derived under the assumption that the dynamics never introduce any coherences between the zero- and single-excitation subspaces. This is the case here, since the unitary evolution is restricted to the single-excitation subspace. Subtracting Eq. (5.30) from Eq. (5.31), we get

$$E_R - D = S(\Delta) - S(\rho^B) - \min_{\{\Pi_j^B\}}[p_1 S(\rho^{A|\Pi_1^B}) - p_2 S(\rho^{A|\Pi_2^B})]. \tag{5.32}$$

It turns out that this expression is independent of the phase angle ϕ. This is reasonable, since ϕ only appears in the coherence between the ground and excited state. Moreover, the last term is minimal for $\theta = \frac{n\pi}{2}$ (cf. Appendix A.4). This means that the optimal measurement operators are projectors onto the ground and excited states of subsystem B. For the sake of simplicity, we restrict subsystem A to consist of only two sites. This is enough to quantify the quantum correlations between two entry sites and the trapping site. By specifying the basis for the reduced bipartite system (here e.g. A=1,2 and B=3),

$$\begin{pmatrix}1\\0\\0\\0\end{pmatrix} = |g\rangle_1 |g\rangle_2 |g\rangle_3, \quad \begin{pmatrix}0\\1\\0\\0\end{pmatrix} = |e\rangle_1 |g\rangle_2 |g\rangle_3, \tag{5.33}$$

$$\begin{pmatrix}0\\0\\1\\0\end{pmatrix} = |g\rangle_1 |e\rangle_2 |g\rangle_3, \quad \begin{pmatrix}0\\0\\0\\1\end{pmatrix} = |g\rangle_1 |g\rangle_2 |e\rangle_3, \tag{5.34}$$

we can give explicit expressions for the various matrices involved:

$$\Delta = \begin{pmatrix} 1-(\rho_{\alpha\alpha}+\rho_{\beta\beta}+\rho_{\gamma\gamma}) & 0 & 0 & 0 \\ 0 & \rho_{\alpha\alpha} & \rho_{\alpha\beta} & 0 \\ 0 & \rho_{\beta\alpha} & \rho_{\beta\beta} & 0 \\ 0 & 0 & 0 & \rho_{\gamma\gamma} \end{pmatrix}, \tag{5.35}$$

$$\rho^B = \begin{pmatrix} 1-\rho_{\gamma\gamma} & 0 \\ 0 & \rho_{\gamma\gamma} \end{pmatrix}, \tag{5.36}$$

$$\rho^{A|\Pi_1^B} = \frac{1}{p_1}\begin{pmatrix} 1-(\rho_{\alpha\alpha}+\rho_{\beta\beta}+\rho_{\gamma\gamma}) & 0 & 0 \\ 0 & \rho_{\alpha\alpha} & \rho_{\alpha\beta} \\ 0 & \rho_{\beta\alpha} & \rho_{\beta\beta} \end{pmatrix}, \tag{5.37}$$

$$\rho^{A|\Pi_2^B} = \frac{1}{p_2}\begin{pmatrix} \rho_{\gamma\gamma} & 0 & 0 \\ 0 & 0 & 0 \\ 0 & 0 & 0 \end{pmatrix}, \tag{5.38}$$

where $p_1 = 1-\rho_{\gamma\gamma}$ and $p_2 = \rho_{\gamma\gamma}$. The greek indices α and β denote the sites in A, while γ stands for the site in B. To calculate the entropies, we note that
$S(X) = -X\log_2(X) = -\sum_i \lambda_i \log_2(\lambda_i)$, where $\{\lambda_i\}$ are the eigenvalues of X, and define

$$\lambda_1 = 1-(\rho_{\alpha\alpha}+\rho_{\beta\beta}+\rho_{\gamma\gamma}) \tag{5.39}$$

$$\lambda_{2/3} = \text{Eigenvalues}\begin{pmatrix} \rho_{\alpha\alpha} & \rho_{\alpha\beta} \\ \rho_{\beta\alpha} & \rho_{\beta\beta} \end{pmatrix} \tag{5.40}$$

$$\lambda_4 = \rho_{\gamma\gamma}. \tag{5.41}$$

Therefore, $S(\Delta) = -\sum_i \lambda_i \log_2(\lambda_i)$ and $S(\rho^B) = -(1-\rho_{\gamma\gamma})\log_2(1-\rho_{\gamma\gamma}) - \lambda_4\log_2(\lambda_4)$. Next, we consider the last two terms of Eq. (5.32),

$$p_1 S(\rho^{A|\Pi_1^B}) = -\sum_{i=1}^{3} \lambda_i \log_2(\frac{\lambda_i}{p_1}) \tag{5.42}$$

$$= -\sum_{i=1}^{3} \lambda_i \log_2(\lambda_i) + (\lambda_1+\lambda_2+\lambda_3)\log_2(p_1) \tag{5.43}$$

$$= (1-\rho_{\gamma\gamma})\log_2(1-\rho_{\gamma\gamma}) - \sum_{i=1}^{3} \lambda_i \log_2(\lambda_i) \tag{5.44}$$

and

$$p_2 S(\rho^{A|\Pi_2^B}) = -\rho_{\gamma\gamma}\log_2(\frac{\rho_{\gamma\gamma}}{\rho_{\gamma\gamma}}) \tag{5.45}$$

$$= -\rho_{\gamma\gamma}\log_2(1) \tag{5.46}$$

$$= 0. \tag{5.47}$$

Plugging everything back into Eq. (5.32), we end up with

$$E_R - D = -\sum_{i=1}^{4} \lambda_i \log_2(\lambda_i) + (1-\rho_{\gamma\gamma}) \log_2(1-\rho_{\gamma\gamma}) + \lambda_4 \log_2(\lambda_4) \tag{5.48}$$

$$- (1-\rho_{\gamma\gamma}) \log_2(1-\rho_{\gamma\gamma}) + \sum_{i=1}^{3} \lambda_i \log_2(\lambda_i) = 0, \tag{5.49}$$

and therefore $E_R(\rho^{AB}) = D(\rho^{AB})$.

5.2.2 Conclusion

In conclusion, we found that the global versions of quantum discord and relative entropy of entanglement agree in the single-excitation subspace because the separable states are exactly the classical states in this context. Further, we proved that the bipartite versions also match. Before, this was only suggested by numerical investigations by Brádler *et al.* (2010). In the derivation of Eq. (5.31) from Brádler *et al.* (2010) and in the computation of the matrices (5.37) and (5.38) the assumption that there are no coherences between the zero- and single-excitation subspace was used. This could be the crucial point which restricts the application of this proof. In contrast, the restriction in the number of sites (at least for subsystem A) was just for convenience, and there is no problem in relaxing this assumption. Since we have seen that entanglement is equivalent to coherence in the site basis, we can now extend this equivalence also to quantum discord. This can also be seen directly in the Eqs. (5.31) and (5.35). If all coherences vanish, then $\rho^{AB} = \Delta(\rho^{AB})$, and $E_R = 0 = D$. However in Section , we will see that the logarithmic negativity does not coincide with quantum discord.

It is worth mentioning that while the definition of the relative entropy of entanglement was restricted to the zero- and single-excitation subspace and the resulting formula is only valid in this case, the definition of quantum discord is general. But the restriction is hidden in the fact that we fixed subsystem B to only consist of one site. Therefore, the optimization is effectively restricted to the zero- and single-excitation subspace. Brádler *et al.* (2010) calculated the relative entropy of entanglement also taking into account double excitations and found that the entanglement decreases significantly if the state has only a very small part that lies beyond the single excitation subspace. This effect cannot be captured with our definition of quantum discord.

5.3 Dynamics of Classical and Quantum Correlations

In the last section we recognized that the relative entropy of entanglement and the quantum discord coincide for our model of excitation transport in the single-excitation domain. Further, we saw that we can omit the optimization procedure inherent in the computation of quantum discord and relative entropy of entanglement. This insight allows us to study the dynamics for a large set of parameters.

In the following, we consider the question if there is a relationship between the efficiency and the occurrence of classical and quantum correlations. The quantum correlations are quantified by the bipartite relative entropy of entanglement and the classical correlations by the difference of the total correlations - measured by the mutual information - and the quantum correlations. As already mentioned in the last section, we consider the situation where subsystem A consists of the sites that are excited initially, A=1,2 or A=1,6, and subsystem B consists of the trapping site, B=3 or B=4.

5.3.1 Superpositions of $|1\rangle$ and $|2\rangle$

We start with the states $|best\rangle$ and $|worst\rangle$ Eq. (4.5). Therefore, the system AB is defined to consist of sites 1, 2 and 3. In Figs. 5.3 and 5.4, the time evolution of the correlations is shown. The green, dashed line represents the total correlations, the blue solid line the quantum correlations, and the red, dotted line the classical correlations. Each of the three plots in the Figs. corresponds to a fixed dephasing rate, (a) corresponds to $\gamma = 0.1\,\mathrm{ps}^{-1}$, (b) to $\gamma = 1\,\mathrm{ps}^{-1}$, and (c) to $\gamma = 10\,\mathrm{ps}^{-1}$. Remarkably, even for dephasing with rate $1\,\mathrm{ps}^{-1}$, the quantum correlations exceed the classical correlations. Comparing Figs. 5.3(a) and 5.4(a), we notice that the correlations in the optimal case are a factor of approximately 5 higher than in the pessimal case. But this is only holds for very low dephasing. While dephasing leads to a decay of correlations for $|best\rangle$, almost the opposite is true for $|worst\rangle$. Here, only the quantum correlations loose strength. On the other hand, classical correlations become stronger. In fact, while the correlations loose structure with increasing dephasing, the total correlations become more pronounced due to the classical correlations. Anyhow, for those marginal initial states, with respect to efficiency for zero dephasing, we see high efficiency goes hand in hand with stronger correlations. But the increase of the efficiency for dephasing rates about $10\,\mathrm{ps}^{-1}$ cannot be understood by looking at the correlations.

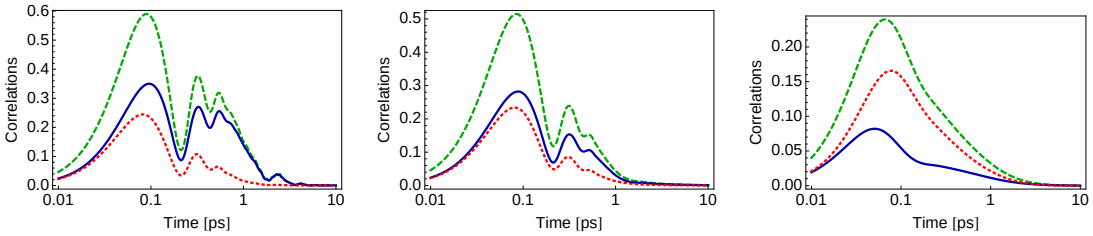

(a) $\gamma = 0.1\ ps^{-1}$ (b) $\gamma = 1\ ps^{-1}$ (c) $\gamma = 10\ ps^{-1}$

Figure 5.3: The green, dashed line represents the total correlations, the blue, solid line the quantum correlations, and the red, dotted line the classical correlations.The initial state is $|best\rangle$ (cf. (4.5)). Subsystem A consists of sites 1 and 2, subsystem B of site 3. Trapping is at site 3 with rate $5\,\mathrm{ps}^{-1}$.

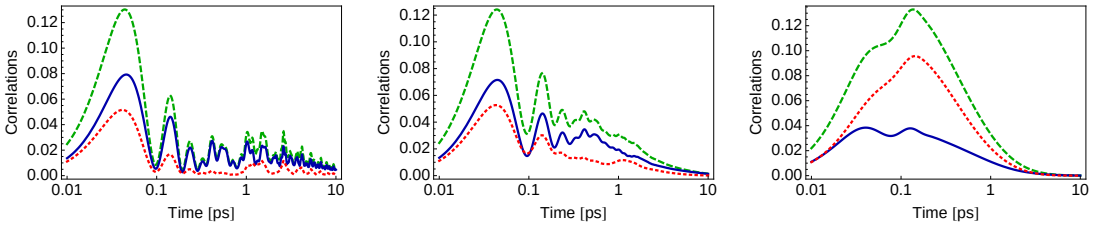

(a) $\gamma = 0.1\ ps^{-1}$ (b) $\gamma = 1\ ps^{-1}$ (c) $\gamma = 10\ ps^{-1}$

Figure 5.4: The green, dashed line represents the total correlations, the blue line the quantum correlations, and the red, pointed line the classical correlations. The initial state is $|worst\rangle$ (cf. (4.5)). Subsystem A consists of sites 1 and 2, subsystem B of site 3. Trapping is at site 3 with rate $5\,\mathrm{ps}^{-1}$.

Figs. 5.5 and 5.6 show the dependence on the dephasing rate in more detail. Again, in all cases quantum correlations decay with increasing dephasing. We will explain this observation in a moment.

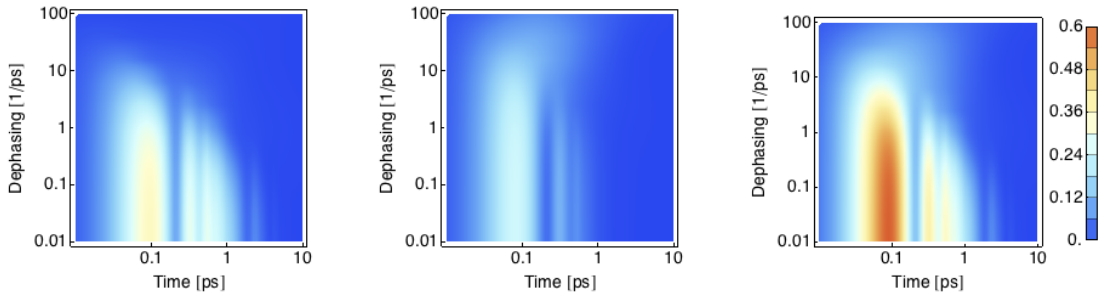

(a) Quantum Correlations. (b) Classical Correlations. (c) Total Correlations.

Figure 5.5: The initial state is $|best\rangle$ (cf. (4.5)). Trapping is at site 3 with rate $5\,\mathrm{ps}^{-1}$.

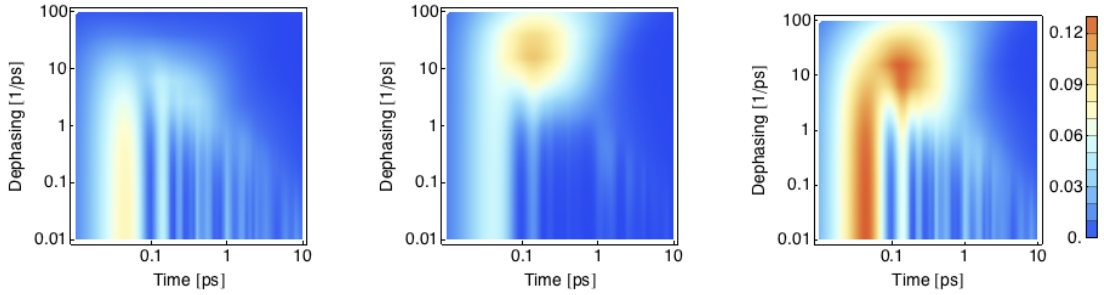

(a) Quantum Correlations. (b) Classical Correlations. (c) Total Correlations.

Figure 5.6: The initial state is $|worst\rangle$ (cf. (4.5)). Trapping is at site 3 with rate $5\,\mathrm{ps}^{-1}$.

In the last chapter, we found out that the appearance of quantum correlations in the single-excitation subspace is closely related to the existence of coherences in the site basis. Therefore, we try to explain the dynamics of quantum correlations with those of the coherences. In the present case, the contributing coherences between subsystem A and B are ρ_{13} and ρ_{23}. Thus, we define a measure of bipartite coherence by

$$C_{AB} = \frac{1}{2} \sum_{i \neq j} |\rho_{ij}|, \tag{5.50}$$

where i labels sites in A and j labels sites in B.

If we compare the behavior of the quantum correlations in Figs. 5.3 and 5.4 with that of Figs. 5.7(a) and 5.7(b), we recognize that $C_{12,3}$ resembles the structure of the quantum

correlations intriguingly. Still, we can not match the lines by rescaling with a constant factor. But now we are in the position to explain the observed decay of quantum correlations by the action of the Lindblad pure dephasing term that leads to an exponential decay of the coherences. We note that in the coherence measure only the coherences between the two subsystems A and B take part. Therefore, we cannot directly evoke a connection between coherence in the initial condition and the appearance of quantum correlations, since these are coherences inherent in a single subsystem.

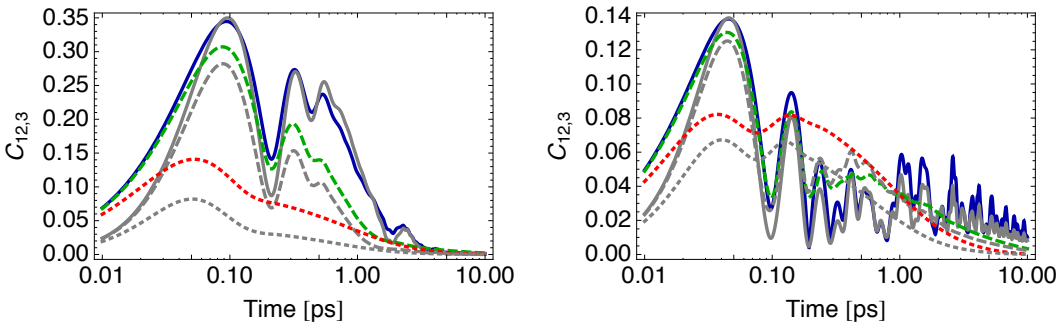

(a) The initial state is $|best\rangle$.

(b) The initial state is $|worst\rangle$.

Figure 5.7: Plot of the coherence measure C_{AB} (5.50). The blue, solid line represents γ = $0.1\,\mathrm{ps}^{-1}$, the green, dashed line γ = $1\,\mathrm{ps}^{-1}$, and the red, dotted line γ = $10\,\mathrm{ps}^{-1}$. The grey lines represent the respective quantum correlations from Fig. 5.3. These are scaled by a factor of 1.75 in the right Figure. Subsystem A consists of sites 1 and 2, subsystem B of site 3. Trapping is at site 3 with rate $5\,\mathrm{ps}^{-1}$.

Having discussed the origin of the quantum correlations, we proceed with the classical correlations. It is known that a pure state cannot be correlated with another system. For this reason, it is tempting to compare the total correlations with the purity of the subsystems, which is defined by

$$P(\rho) = \mathrm{tr}(\rho^2), \tag{5.51}$$

and ranges from 1 for pure states to $1/\dim(\rho)$ for totally mixed states. For better comparison we calculate $1 - P(\rho)$, which is equivalent to a quantity called linear entropy. It turns out that the purity of subsystem B is more informative in this case. If we compare Fig. 5.8 with the classical correlations in Figs. 5.3 and 5.4, we recognize a resemblance of the shape, although there is a bit more structure in the purity measure. This resemblance is especially good for low dephasing and short times. While the peaks do not agree in magnitude, their location in time does quite well. Against my expectations, the correlations disappear before the subsystem reaches a pure state. But strikingly, the behavior of the classical correlations with increasing dephasing is captured by the purity. If the initial

state is $|best\rangle$ (Fig. 5.3), the classical correlations are very similar for $\gamma = 0.1\,\mathrm{ps}^{-1}$ and $\gamma = 1\,\mathrm{ps}^{-1}$ and are smaller for $\gamma = 10\,\mathrm{ps}^{-1}$. The same behavior can be seen in Fig. 5.8(a). If the initial state is $|worst\rangle$ (Fig. 5.4), the coincidence of the first peaks, before t = 0.1 ps, in Figs. 5.4(a) and 5.4(b), as well as the increase of the classical correlations with increasing dephasing is reflected in Fig. 5.6. This is all the more surprising, since $P(\rho^B)$ can be written as function of only the population of the site that forms B.

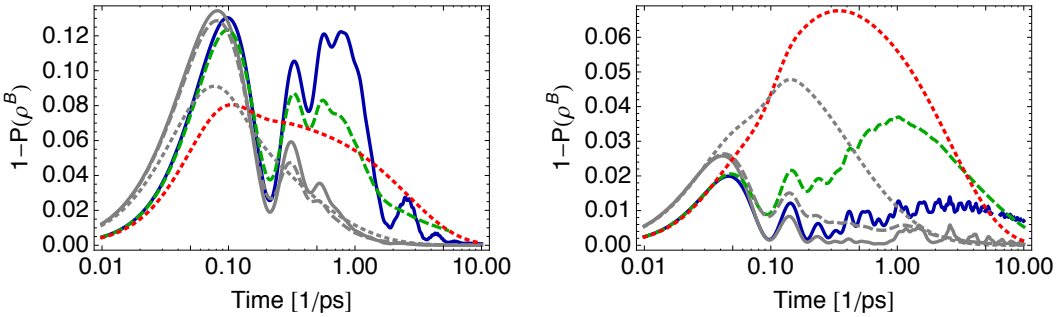

(a) The initial state is $|best\rangle$.

(b) The initial state is $|worst\rangle$.

Figure 5.8: Plot of $1 - P(\rho^B)$ (5.51). The blue, solid line represents $\gamma = 0.1\,\mathrm{ps}^{-1}$, the green, dashed line $\gamma = 1\,\mathrm{ps}^{-1}$, and the red, dotted line $\gamma = 10\,\mathrm{ps}^{-1}$. The grey lines represent the respective classical correlations scaled by constant factors. Subsystem B consists of site 3. Trapping is at site 3 with rate $5\,\mathrm{ps}^{-1}$.

5.3.2 Superpositions of $|1\rangle$ and $|6\rangle$

We continue with the **opt**imal and **pes**simal superpositions of $|1\rangle$ and $|6\rangle$. This won't bring any new insights, but supports the findings of the preceding section.

Again, we see (Figs. 5.9 and 5.10) that especially the quantum correlations are more pronounced for an initial state of $|opt\rangle$. Also the decay of quantum correlations is visible in both cases. Different from the superpositions of $|1\rangle$ and $|2\rangle$, the strongest peak appears after 100 fs. This is because sites 1 and 2 are coupled stronger to site 3 than sites 1 and 6 to site 4.

The connection between the quantum correlations and our coherence measure (5.50) is not as distinct as before, but can nevertheless be observed (Fig. 5.11). The same is true for the purity and the classical correlations (Figs. 5.12 and 5.13).

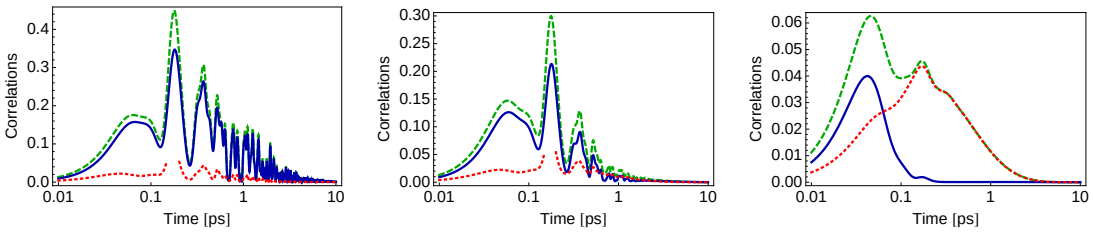

(a) $\gamma = 0.1\,\mathrm{ps}^{-1}$ (b) $\gamma = 1\,\mathrm{ps}^{-1}$ (c) $\gamma = 10\,\mathrm{ps}^{-1}$

Figure 5.9: The green, dashed line represents the total correlations, the blue line the quantum correlations, and the red, pointed line the classical correlations. The initial state is $|opt\rangle$ (see Fig. 4.10(b)). Subsystem A consists of sites 1 and 6, subsystem B of site 4. Trapping is at site 4 with rate $5\,\mathrm{ps}^{-1}$. The dropout in the classical correlations are an unknown artifact stemming from the computation with *Mathematica*. Since the classical correlations are the difference of the total and the quantum correlations, the missing values are uniquely defined.

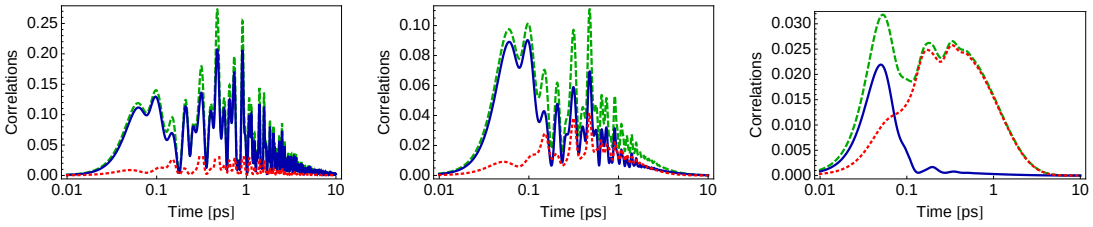

(a) $\gamma = 0.1\,\mathrm{ps}^{-1}$ (b) $\gamma = 1\,\mathrm{ps}^{-1}$ (c) $\gamma = 10\,\mathrm{ps}^{-1}$

Figure 5.10: The green, dashed line represents the total correlations, the blue line the quantum correlations, and the red, pointed line the classical correlations. The initial state is $|pes\rangle$ (cf. Fig. 4.10(b)). Subsystem A consists of sites 1 and 6, subsystem B of site 4. Trapping is at site 4 with rate $5\,\mathrm{ps}^{-1}$.

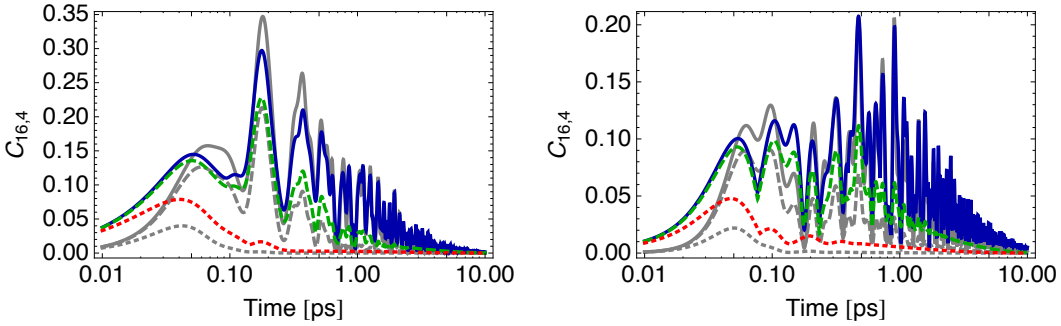

(a) The initial state is $|opt\rangle$. (b) The initial state is $|pes\rangle$.

Figure 5.11: Plot of the coherence measure C_{AB} (5.50). The blue, solid line represents $\gamma = 0.1\,\mathrm{ps}^{-1}$, the green, dashed line $\gamma = 1\,\mathrm{ps}^{-1}$, and the red, dotted line $\gamma = 10\,\mathrm{ps}^{-1}$. The gray lines represent the corresponding quantum correlations. Subsystem A consists of sites 1 and 6, subsystem B of site 4. Trapping is at site 4 with rate $5\,\mathrm{ps}^{-1}$.

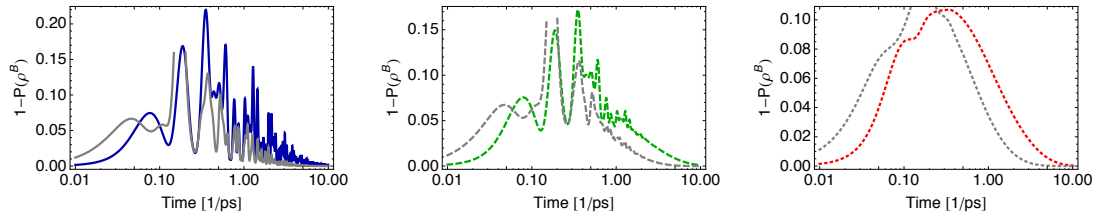

(a) $\gamma = 0.1\,\mathrm{ps}^{-1}$ (b) $\gamma = 1\,\mathrm{ps}^{-1}$ (c) $\gamma = 10\,\mathrm{ps}^{-1}$

Figure 5.12: The colored lines represent $1-P(\rho^B)$, the gray lines the classical correlations scaled by a factor of three. The initial state is $|opt\rangle$ (cf. Fig. 4.10(b)). Subsystem A consists of sites 1 and 6, subsystem B of site 4. Trapping is at site 4 with rate $5\,\mathrm{ps}^{-1}$.

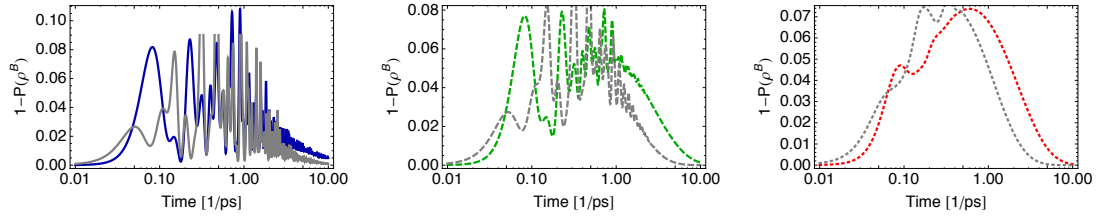

(a) $\gamma = 0.1\,\mathrm{ps}^{-1}$ (b) $\gamma = 1\,\mathrm{ps}^{-1}$ (c) $\gamma = 10\,\mathrm{ps}^{-1}$

Figure 5.13: The colored lines represent $1-P(\rho^B)$, the gray lines the classical correlations scaled by a factor of three. The initial state is $|pes\rangle$ (cf. Fig. 4.10(b)). Subsystem A consists of sites 1 and 6, subsystem B of site 4. Trapping is at site 4 with rate $5\,\mathrm{ps}^{-1}$.

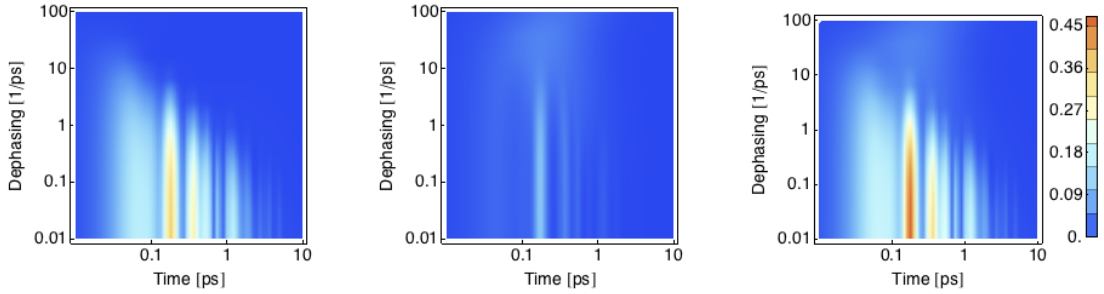

(a) Quantum Correlations. (b) Classical Correlations. (c) Total Correlations.

Figure 5.14: The initial state is $|opt\rangle$ (cf. Fig. 4.10(b)). Subsystem A consists of sites 1 and 6, subsystem B of site 4. Trapping is at site 4 with rate $5\,\mathrm{ps}^{-1}$.

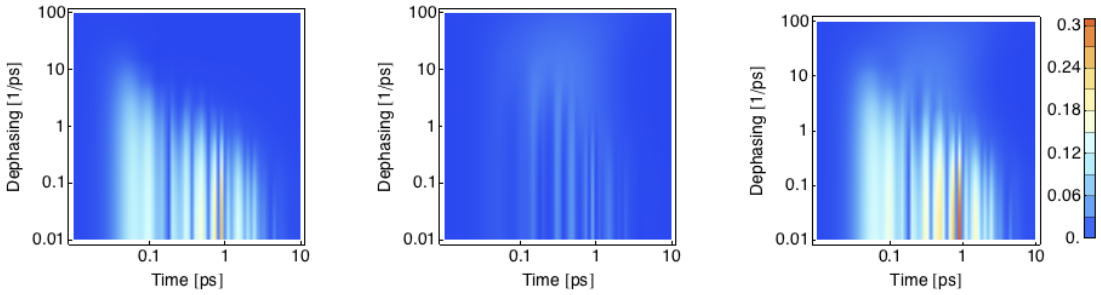

(a) Quantum Correlations. (b) Classical Correlations. (c) Total Correlations.

Figure 5.15: The initial state is $|pes\rangle$ (cf. Fig. 4.10(b)). Subsystem A consists of sites 1 and 6, subsystem B of site 4. Trapping is at site 4 with rate $5\,\mathrm{ps}^{-1}$.

5.3.3 Conclusion

In this section, we compared the time evolution of quantum and classical correlations, as well as their dependence of dephasing for the initial superpositions $|best\rangle$ ($|opt\rangle$) and $|worst\rangle$ ($|pes\rangle$) defined in Sec. 4.2.1 (4.2.2). These are superpositions of the states $|1\rangle$ and $|2\rangle$ ($|6\rangle$) which lead to highest (lowest) efficiency for zero dephasing. We have seen that the correlations in the state arising from the high-efficiency initial condition exceed those of the state arising from the low-efficiency condition. But the maximum of efficiency around $\gamma = 10\,\mathrm{ps}^{-1}$, shared by all considered states, is not reflected in the correlations. The only hint could be the rise of classical correlations that occurs around $\gamma = 10\,\mathrm{ps}^{-1}$ and t = 0.1 ps (Figs. 5.6(b) and 5.5(b)), but this is rather questionable. The striking result of this section is the close link between the quantum correlations and the coherences between the subsystems, and between the classical correlations and the purity of subsystem B.

5.4 Brief Glimpse Beyond Single Excitations

So far, we concentrated on the zero- and single-excitation subspace. This restriction is usually justified by the argument of weak incoming sunlight. But this argument has some flaws. Even if the irradiation is weak, it is nevertheless artificial to assume an initial state of exactly one excitation, similar to a quantum mechanical Fock state Tiersch *et al.* (2011). Moreover, the wave-like behavior observed in the experiments was under laser excitation which is a highly-potent light source.

In this section, we leave our main path. During this thesis we have mainly discussed consequences of non-local superpositions between single excitations in the initial state. Now, we compare the evolution of quantum discord and entanglement as measured by the logarithmic negativity (Sec. 5.1.1) for the case of no initial coherences in the site basis as well as with coherences. Thus, we won't contribute new insights to answer our main questions, but are able to investigate the following intriguing questions:

1. Does quantum discord only appear hand in hand with entanglement?
2. Is coherence in the initial state connected to greater correlations and entanglement?
3. Which role does the probability of higher excitations play?

5.4.1 Method

We take the simplest approach to include higher excitations. We neglect additional processes like exciton-exciton scattering and hold on to the two-level system. Thus, we remove the single-excitation restriction by replacing the ladder operators[†] (e.g. in Eq. (3.6)) with

$$\sigma_i^{+/-} = \mathbb{1} \otimes \cdots \otimes \mathbb{1} \otimes \underbrace{\tilde{\sigma}^{+/-}}_{i\text{th place}} \otimes \mathbb{1} \otimes \cdots \otimes \mathbb{1}, \tag{5.52}$$

where $\mathbb{1}$ is the two-dimensional identity operator and $\tilde{\sigma}^{+/-}$ are the two-dimensional ladder operators $\tilde{\sigma}^{+} = |e\rangle\langle e|$ and $\tilde{\sigma}^{-} = |g\rangle\langle g|$. This increases the number of coupled differential equations from 7+1 to 2^{7+1}=256. But besides the dissipation and trapping process, the number of excitations is conserved. In particular, the number of excitations does not increase during the time evolution. Knowing this, we conclude that there will be no more excitations in the system than initially excited. Therefore, we extract only the differential equations of the subspaces given by the initial condition. In what follows, we consider again two entry sites and end up with $\binom{8}{0} + \binom{8}{1} + \binom{8}{2} = 1 + 8 + 28 = 37$ equations.

5.4.2 Initial Condition

We consider two types of initial conditions. In each case, the initial state is completely separable with respect to partitioning the system into subsystems consisting of one site.

[†]The system Hamiltonian H_S (3.1) can also be rewritten in terms of ladder operators.

The sites which are not entry sites are in the ground state, and the entry sites are in one of the following states,

$$\rho_{init,c} = \frac{1}{1+\alpha^2}(|g\rangle\langle g| + \alpha|g\rangle\langle e| + \alpha|e\rangle\langle g| + \alpha^2|e\rangle\langle e|) \tag{5.53}$$

or

$$\rho_{init,nc} = \frac{1}{1+\alpha^2}(|g\rangle\langle g| + \alpha^2|e\rangle\langle e|). \tag{5.54}$$

The c respective nc stands for *(non-) coherent*. Indeed, Eq. (5.53) has the form of a coherent state Zhang *et al.* (1990) for a two-level system. In both states the probability to find one or two excitations in the system is scaled by the parameter α. For $\alpha > 1$, it is most probable to find the system in a double excited state, for $\alpha < 1$, the ground state is preferred. If $\alpha = 1$, no excitation, one excitation and two excitations are equally probable. We note that not only the probability of higher excitations is new, but also the probability to have no excitation.

The initial state is then built-up by Kronecker products of ground state density matrices and Eq. (5.53) or (5.54). For coherent states at sites 1 and 6 for example, the initial state is

$$\rho_{init,c12} = \rho_{init,c} \otimes \rho_g \otimes \rho_g \otimes \rho_g \otimes \rho_g \otimes \rho_{init,c} \otimes \rho_g \otimes \rho_g, \tag{5.55}$$

where $\rho_g = |g\rangle\langle g|$ denotes the ground state density matrix of a site.

5.4.3 Dynamics

Entry sites 1 and 6

We restrict the discussion to the situation where sites 1 and 6 are considered as the entry sites and site 4 is connected to the trap. Figs. 5.16-5.20 show the evolution of quantum discord, mutual information and logarithmic negativity for (non-) coherent initial conditions, various α and various dephasing rates γ.

To answer the first question, if quantum discord appears only together with entanglement as in the zero- and single-excitation subspaces, we just have to compare the Figs. 5.16 and 5.18 as well as Figs. 5.17 and 5.20. At first sight, we note that the range of non-zero quantum discord is typically larger than that of non-zero logarithmic negativity. Remarkably, in the coherent case the logarithmic negativity exceeds quantum discord for α and

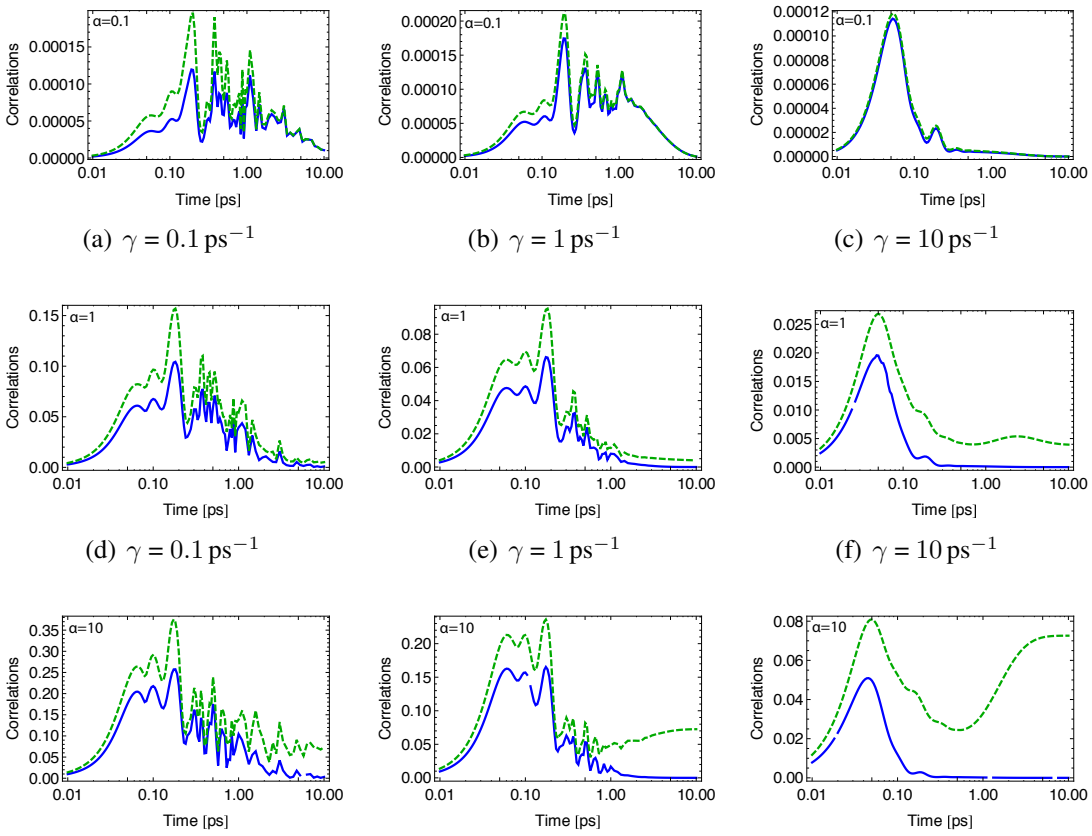

(a) $\gamma = 0.1\,\mathrm{ps}^{-1}$ (b) $\gamma = 1\,\mathrm{ps}^{-1}$ (c) $\gamma = 10\,\mathrm{ps}^{-1}$

(d) $\gamma = 0.1\,\mathrm{ps}^{-1}$ (e) $\gamma = 1\,\mathrm{ps}^{-1}$ (f) $\gamma = 10\,\mathrm{ps}^{-1}$

(g) $\gamma = 0.1\,\mathrm{ps}^{-1}$ (h) $\gamma = 1\,\mathrm{ps}^{-1}$ (i) $\gamma = 10\,\mathrm{ps}^{-1}$

Figure 5.16: Quantum discord (blue) and mutual information (green, dashed) for initial coherent states at site 1 and site 6. Trapping is at site 4 with rate $5\,\mathrm{ps}^{-1}$.

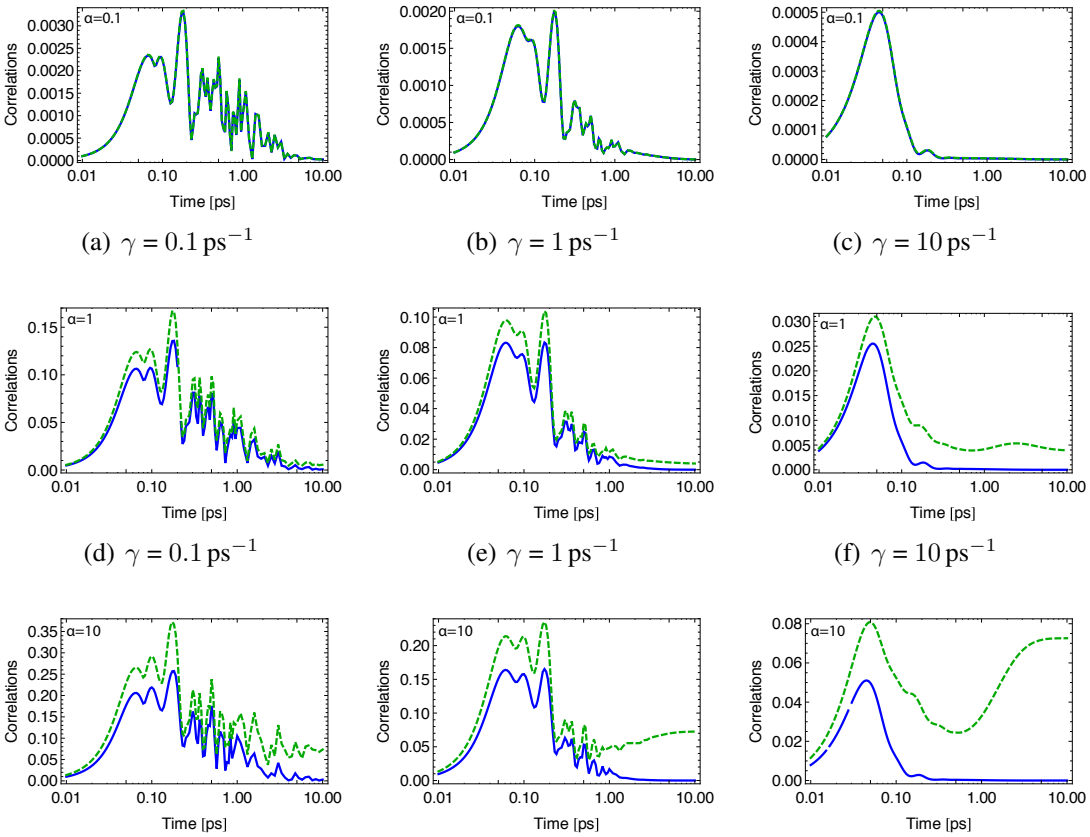

(a) $\gamma = 0.1\,\mathrm{ps}^{-1}$ (b) $\gamma = 1\,\mathrm{ps}^{-1}$ (c) $\gamma = 10\,\mathrm{ps}^{-1}$

(d) $\gamma = 0.1\,\mathrm{ps}^{-1}$ (e) $\gamma = 1\,\mathrm{ps}^{-1}$ (f) $\gamma = 10\,\mathrm{ps}^{-1}$

(g) $\gamma = 0.1\,\mathrm{ps}^{-1}$ (h) $\gamma = 1\,\mathrm{ps}^{-1}$ (i) $\gamma = 10\,\mathrm{ps}^{-1}$

Figure 5.17: Quantum discord (blue) and mutual information (green, dashed) for initial non-coherent states at site 1 and site 6. Trapping is at site 4 with rate $5\,\mathrm{ps}^{-1}$.

γ equal to 0.1 and 1 (Figs. 5.16(a), 5.16(b), 5.16(d), 5.16(e), 5.18(a), 5.18(b), 5.18(d) and 5.18(e)). Although we have introduced quantum discord as a more general measure of quantum correlations than entanglement, we have to admit that there is no universal ordering relation. Ali *et al.* (2010) found this for general two-qubit X states. In all other cases quantum discord is greater than logarithmic negativity. Moreover, especially for γ = 1 ps^{-1} the evolution of logarithmic negativity reminds of sudden death of entanglement Yu and Eberly (2009) around t = 1 ps. In contrast, the evolution of quantum discord follows an asymptotic decay. In summary, the answer to the first question is *no*. The time evolution of quantum discord and logarithmic negativity is distinct. Since this is also very explicit for small α, not only the higher excitations but the probability of no excitation could be responsible.

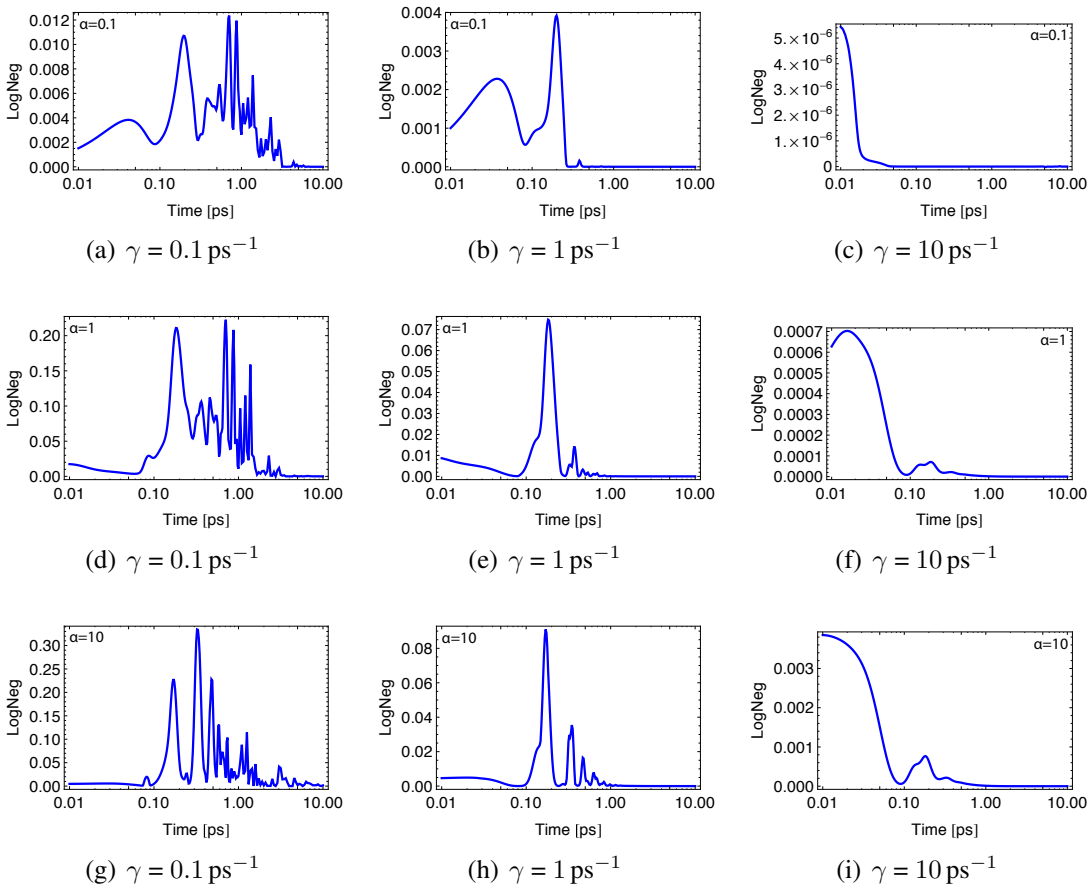

(a) $\gamma = 0.1\,\mathrm{ps}^{-1}$ (b) $\gamma = 1\,\mathrm{ps}^{-1}$ (c) $\gamma = 10\,\mathrm{ps}^{-1}$

(d) $\gamma = 0.1\,\mathrm{ps}^{-1}$ (e) $\gamma = 1\,\mathrm{ps}^{-1}$ (f) $\gamma = 10\,\mathrm{ps}^{-1}$

(g) $\gamma = 0.1\,\mathrm{ps}^{-1}$ (h) $\gamma = 1\,\mathrm{ps}^{-1}$ (i) $\gamma = 10\,\mathrm{ps}^{-1}$

Figure 5.18: Entanglement measured by logarithmic negativity for initial coherent states at site 1 and site 6. Trapping is at site 4 with rate $5\,\mathrm{ps}^{-1}$.

The answer of the second question is very surprising. Here, the non-coherent initial condition surpasses the coherent one in terms of quantum discord for α equal to 0.1 and 1.

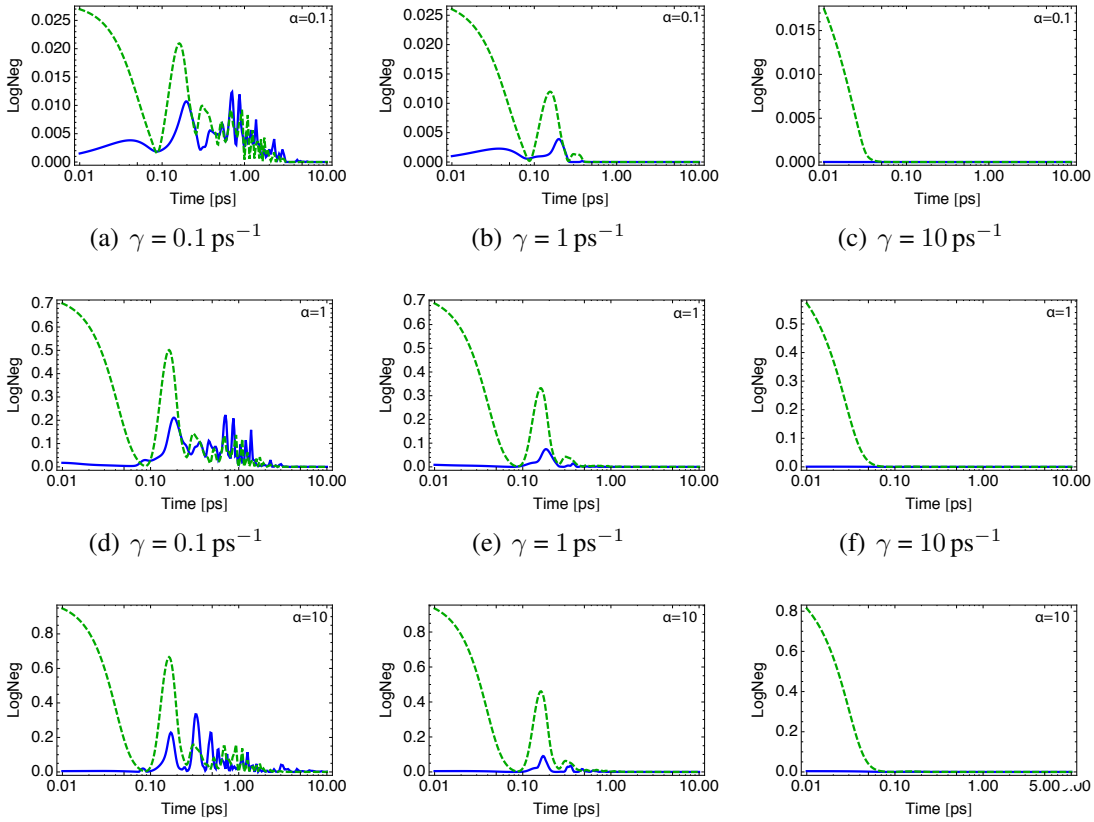

(a) $\gamma = 0.1\,\mathrm{ps}^{-1}$ (b) $\gamma = 1\,\mathrm{ps}^{-1}$ (c) $\gamma = 10\,\mathrm{ps}^{-1}$

(d) $\gamma = 0.1\,\mathrm{ps}^{-1}$ (e) $\gamma = 1\,\mathrm{ps}^{-1}$ (f) $\gamma = 10\,\mathrm{ps}^{-1}$

(g) $\gamma = 0.1\,\mathrm{ps}^{-1}$ (h) $\gamma = 1\,\mathrm{ps}^{-1}$ (i) $\gamma = 10\,\mathrm{ps}^{-1}$

Figure 5.19: Logarithmic negativity with (blue) and without (green, dashed) double excitations for initial coherent states at site 1 and site 6. Trapping is at site 4 with rate $5\,\mathrm{ps}^{-1}$.

But even more staggering, for $\alpha = 10$, quantum discord perfectly coincide for both initial states (cf. Figs. 5.16 and 5.17). In the case of logarithmic negativity the agreement is not perfect, but convincing. For $\alpha \leq 1$ we observe the expected behavior: The amount of entanglement is greater for coherent initial states (cf. Figs. 5.18 and 5.20).

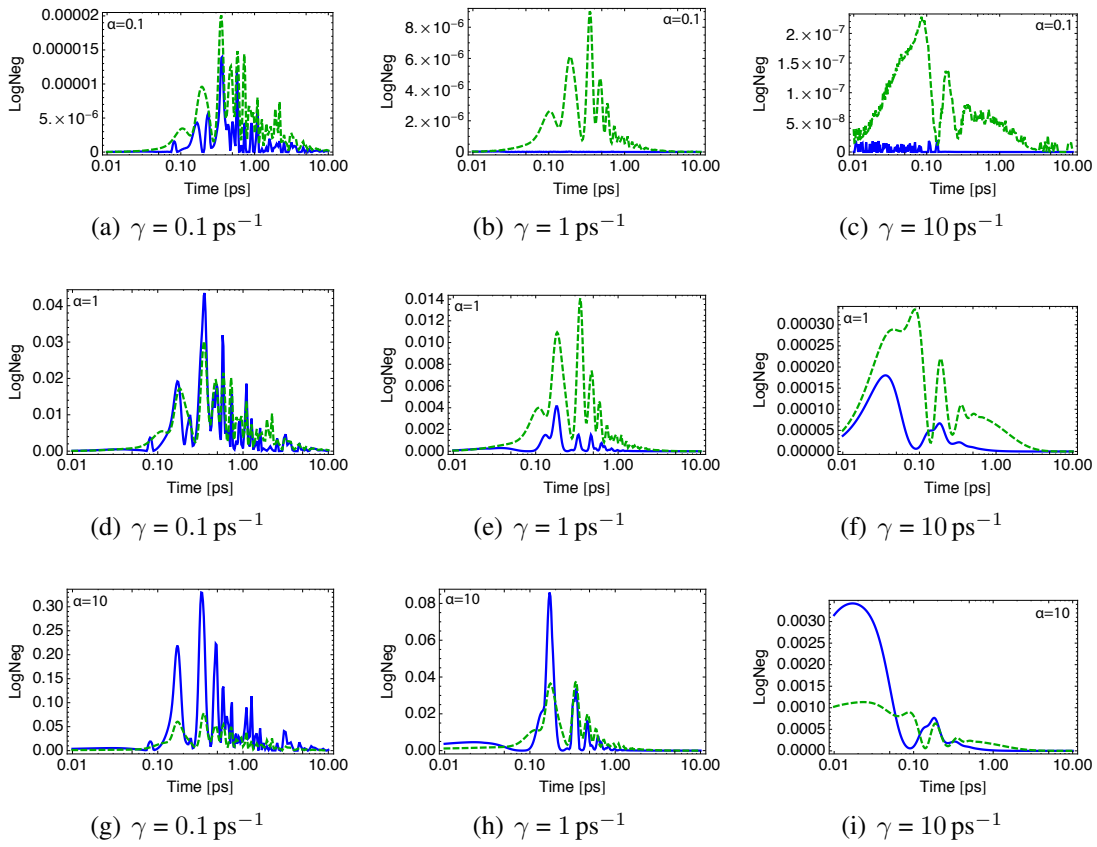

(a) $\gamma = 0.1\,\mathrm{ps}^{-1}$ (b) $\gamma = 1\,\mathrm{ps}^{-1}$ (c) $\gamma = 10\,\mathrm{ps}^{-1}$

(d) $\gamma = 0.1\,\mathrm{ps}^{-1}$ (e) $\gamma = 1\,\mathrm{ps}^{-1}$ (f) $\gamma = 10\,\mathrm{ps}^{-1}$

(g) $\gamma = 0.1\,\mathrm{ps}^{-1}$ (h) $\gamma = 1\,\mathrm{ps}^{-1}$ (i) $\gamma = 10\,\mathrm{ps}^{-1}$

Figure 5.20: Logarithmic negativity with (blue) and without (green, dashed) double excitations for initial non-coherent states at site 1 and site 6. Trapping is at site 4 with rate $5\,\mathrm{ps}^{-1}$.

The third question which tackles the role of higher excitations cannot be entirely answered. If we set the double-excitation part of the initial excitation to zero, the shape of the quantum discord does not change. Only the size decreases by approximately 30% for $\alpha = 1$ and 50% for $\alpha = 10$. For $\alpha = 0.1$, the fraction of double-excitation is too small to cause a significant difference. In contrast, the logarithmic negativity changes significantly. This can be comprehended by comparing the blue and green, dashed lines in Figs. 5.19 and 5.20. Other than quantum discord, logarithmic negativity typically grows if we abandon the double excitations. Only for non-coherent initial states and $\alpha = 10$, double excitations lead to a greater value of logarithmic negativity. We conclude that higher excitations leave the form of quantum discord unchanged, but lead to an increase

of magnitude. However, entanglement, as measured by the logarithmic negativity, is significantly affected by higher excitations. In most cases, the addition of higher excitations causes a decrease of the logarithmic negativity.

There are two more points standing out if we look at quantum discord and mutual information (Figs. 5.16 and 5.17). First, except for $\alpha = 0.1$, we observe a non-zero long-time limit of the mutual information. This is because the model of the reaction center is just another two-level system which is not able to absorb two excitations completely. Thus, the reaction center should be modeled as a $n+1$-level[‡] system or alternatively as a system of n two-level systems.

The second point is the coincidence of quantum discord and mutual information in the case of non-coherent initial conditions and $\alpha = 0.1$. From the last chapter we know this means that all correlations are quantum. If we remember that we have a completely classical initial state, this is very surprising. It has to be connected with the leading probability of zero excitations, but a comprehensible explanation is missing.

In addition, another remark is appropriate. In the foregoing section, we concluded that quantum discord and entanglement is equivalent in the zero- and single-excitation subspace. But this is not true if we quantify entanglement with the logarithmic negativity. Therefore, it would be interesting to repeat the argumentation of this section with the relative entropy of entanglement.

5.4.4 Conclusion

In this section, we included the possibility of double as well as of zero excitations. We saw that the behavior of logarithmic negativity and quantum discord is different. In general, quantum discord is present longer than logarithmic negativity and hence more robust against dephasing. Also, the existence of coherences in the initial state have distinct effects. Coherence-free initial conditions lead to higher discord but lower logarithmic negativity in many cases. The same distinct behavior was observed when we investigated the effect of double excitations. While logarithmic negativity typically drops dramatically when adding a small probability of double excitations, quantum discord, in contrast, increases a little, but perfectly keeps its general form.

[‡] n denotes the number of initial excitations.

6 Summary and Outlook

In this thesis, we investigated the excitation transfer in the Fenna-Matthews-Olson (FMO) complex, which acts as a wire to connect the light-harvesting antenna with the reaction center. We used a simple model of coupled two-level systems, which represent the excitation-carrying pigments (sites), completed by Lindblad terms to include the non-unitary processes of dephasing, exciton recombination and the irreversible transfer to the reaction center (trapping). Since usually it is assumed that the probability of two excitations within one complex is low, we restricted ourselves mainly to the zero- and single-excitation subspaces. We start the summary by taking up the main questions formulated in the introduction:

Can quantum superpositions of localized initial excitations affect the transport efficiency, and is this connected to the appearance of quantum correlations between the entry and exit sites?

We approved the first question in Chapter 4 by investigating essentially three different scenarios:

1. Superposition of localized excitations at sites 1 and 2 and trapping at site 3 (Fig. 6.1(a)),

2. superposition of localized excitations at sites 1 and 2 and trapping at site 4 (Fig. 6.1(b)),

3. superposition of localized excitations at sites 1 and 6 and trapping at site 4 (Fig. 6.1(c)),

where the initial state can be written as

$$|\psi_{init}\rangle = \cos(\theta)\,|\text{First Entry Site}\rangle + \mathrm{e}^{-i\phi}\sin(\theta)\,|\text{Second Entry Site}\rangle\,. \tag{6.1}$$

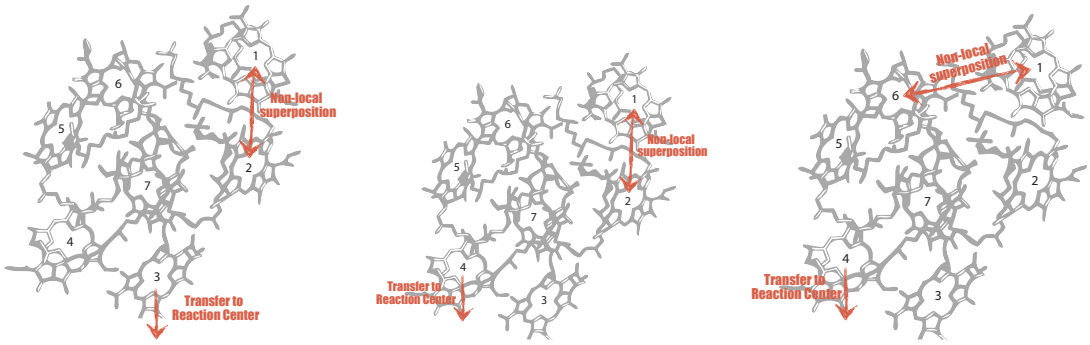

(a) (b) (c)

Figure 6.1: Illustration of the three main excitation transfer scenarios investigated in this thesis.

In all scenarios, we identified superpositions that lead to highest and lowest efficiency for zero dephasing. While other authors emphasized the positive role of dephasing for the efficiency, we conclude that the most efficient transfer is realized *without* dephasing and *with* optimized initial superpositions. In this case the quantum nature is optimally exhausted. Moreover, the efficiency turned out to be quite robust against pure dephasing. Especially if the trapping process takes place at site 4. Additionally, we saw that trapping at site 4 is in most cases beneficial and motivated this by identifying its distinguished connectivity, a quantity, we defined as the sum of the absolute values of the couplings to a specific site. If we assume for a moment that nature optimized the protein scaffold, in which the pigments are embedded, to effectively cool the system in order to prevent dephasing, then we identified a mechanism that could protect the reaction center from overload: For very low dephasing it is possible to modulate the efficiency from 10 % to almost 100 % (Fig. 4.7) by only changing the phase angle ϕ of the initial superposition.

The second question, concerning the effect of quantum correlations, is not easy to answer. Indeed, we found that the dynamics initiated by superpositions leading to highest efficiency give rise to more quantum correlations than the ones initiated by superpositions leading to lowest efficiency. But since we only investigated the marginal cases*, we cannot draw a general conclusion. However, our investigations revealed some other important

*The ones which lead to highest (lowest) efficiency without dephasing.

insights. We have proven that in the zero- and single-excitation subspaces quantum discord and the bipartite version of relative entropy of entanglement coincide, a result that was only shown numerically before. For this proof, the assumption was made that there are no coherences between the zero- and single-excitation subspaces. This is true for the dynamics within our model because the only process that connects the two subspaces is an incoherent recombination process equivalent to spontaneous emission. We also showed the coincidence of the global version of quantum discord, introduced by Modi *et al.* (2010) and the relative entropy of entanglement in the single-excitation subspace. Therefore, we extended the known equivalence between coherence in the site basis and entanglement to quantum discord. This strengthens the conjecture that in the (zero- and) single-excitation subspace all non-classical features are captured within the coherences of the site basis. Moreover, we recognized that the main dynamical features of the quantum correlations are captured by an easy coherence measure. This turned out to be especially fruitful in the first scenario above. In addition, a similar connection between the classical correlations and the purity of one subsystem's density matrix was identified.

In the last section we left the single-excitation subspace and investigated the effect of a new type of initial condition (Sec. 5.4.2) on the dynamics of quantum discord and entanglement as measured by the logarithmic negativity. We found out that quantum discord is typically more robust against dephasing. Also, coherence in the initial condition has different effects on the two measures of quantum correlations. Finally, we pointed out that a small probability of double excitations leads to a drop of the logarithmic negativity together with some structural changes. In contrast, quantum discord even increases without any change in the shape.

As already mentioned in the introduction, the results obtained here should be confirmed in more realistic models. Although the implementation of non-Markovian effects should not change the qualitative picture as shown by Chin *et al.* (2010), it should lead to a delayed decay of coherences and thus also of quantum correlations. Furthermore, our investigations were based on the couplings and site energies of Adolphs and Renger (2006) and could be repeated with values extracted directly from experiments as soon as they are available. Also the 8th pigment could be included.

It would be interesting to see the effects of non-local superpositions of initial conditions on excitation transport also in experiments. This could be achieved by two different approaches. Firstly, experiments in different physical realizations of the transport system like systems of super-conducting qubits Mostame *et al.* (2011), optical cavities Caruso

et al. (2011) and ultracold Rydberg atoms Blumen *et al.* (2007); Weidemüller (2009); Weimer *et al.* (2010) and ions Barreiro *et al.* (2011). Here, the experimentalist has much more influence on the specific parameters and even the environmental interaction can be modeled. Secondly, experiments with the FMO complex using optimal control theory to tailor special-shaped laser pulses that create the desired initial states Brüggemann and May (2004); Brüggemann and Pullerits (2007); Caruso *et al.* (2011).

For the discussion of the role of entanglement and quantum correlations it is vital to perform realistic calculations in the full Hilbert space of arbitrarily many excitations. This is because if we consider a distance-based measure of entanglement[†] like the relative entropy of entanglement, a state that has an arbitrarily small fraction of higher excitations could be far closer to the actual state than the state that is completely confined to the single-excitation subspace Brádler *et al.* (2010). But the complications thereby are twofold: On the one hand of course of the Hilbert space enlarges. Here, we had seven singly-excited states plus one state that represents the reaction center (plus one ground state (cf. Appendix A.1)). Therefore, the dimension of our restricted Hilbert space is 8 (9). Without the restriction, we end up with a dimension of at least 2^7. On the other hand, additional processes have to be included. The most important one is exciton-exciton annihilation. To implement this effect, a three-state model is appropriate which blows up the dimension even more May and Kühn (2011).

[†]Or in principle also more general quantum correlations as well.

7 Bibliography

Abramavicius, D., and S. Mukamel, 2010, J. Chem. Phys. **133**(6), 064510.

Adolphs, J., F. Müh, M. E.-A. Madjet, and T. Renger, 2008, Photosynth. Res. **95**(2-3), 197.

Adolphs, J., and T. Renger, 2006, Biophys. J. **91**(8), 2778.

Ali, M., A. R. P. Rau, and G. Alber, 2010, Phys. Rev. A **81**, 042105.

Arndt, M., T. Juffmann, and V. Vedral, 2009, HFSP J. **3**(6), 386.

Auyuanet, A., and L. Davidovich, 2010, Phys. Rev. A **82**(3).

Ball, P., 2011, Nature **474**(7351), 272.

Barreiro, J. T., M. Müller, P. Schindler, D. Nigg, T. Monz, M. Chwalla, M. Hennrich, C. F. Roos, P. Zoller, and R. Blatt, 2011, Nature **470**(7335), 486.

Barvik, I., and P. Herman, 1992, Phys. Rev. B **45**(6), 2772.

Beatty, J., J. Overmann, M. Lince, A. Manske, A. Lang, R. Blankenship, C. Van Dover, T. Martinson, and F. Plumley, 2005, Proc. Natl. Acad. Sci. USA **102**(26), 9306.

Bell, J., 1964, Physics **1**(3), 195.

Bennett, C. H., G. Brassard, C. Crépeau, R. Jozsa, A. Peres, and W. K. Wootters, 1993, Phys. Rev. Lett. **70**(13), 1895.

Blumen, A., T. Amthor, C. Giese, and M. Reetz-Lamour, 2007, Phys. Rev. Lett. **99**(9), 090601.

Brádler, K., M. M. Wilde, S. Vinjanampathy, and D. B. Uskov, 2010, Phys. Rev. A **82**(6), 062310.

Breuer, H. P., and F. Petruccione, 2007, *The Theory of Open Quantum Systems* (Oxford University Press), ISBN 9780199213900.

Briegel, H. J., and S. Popescu, 2008, ArXiv e-prints arXiv:0806.4552.

Brixner, T., J. Stenger, H. Vaswani, M. Cho, R. Blankenship, and G. Fleming, 2005, Nature **434**(7033), 625.

Brüggemann, B., and V. May, 2004, J. Phys. Chem. **108**(29), 10529.

Brüggemann, B., and T. Pullerits, 2007, J. Photochem. Photobiol. B-Biol. **190**(2-3), 372.

Schmidt am Busch, M., F. Müh, M. El-Amine Madjet, and T. Renger, 2011, J. Phys. Chem. Lett. **2**(2), 93.

Caldeira, A. O., and A. J. Leggett, 1983, Ann. Phys. **149**(2), 374.

Cao, J., 2009, J. Phys. Chem. A. **113**(50), 13825.

Caruso, F., A. Chin, A. Datta, S. Huelga, and M. Plenio, 2010, Phys. Rev. A **81**(6), 62346.

Caruso, F., S. Montangero, T. Calarco, S. F. Huelga, and M. B. Plenio, 2011, ArXiv e-prints arXiv:1103.0929.

Caruso, F., N. Spagnolo, C. Vitelli, F. Sciarrino, and M. Plenio, 2011, Phys. Rev. A **83**(1), 013811.

Cavalcanti, D., L. Aolita, S. Boixo, K. Modi, M. Piani, and A. Winter, 2011, Phys. Rev. A **83**(3), 032324.

Cheng, Y.-C., and G. R. Fleming, 2009, Annu. Rev. Phys. Chem. **60**(1), 241.

Chin, A. W., A. Datta, F. Caruso, S. F. Huelga, and M. B. Plenio, 2010, New J. Phys. **12**(6), 065002+.

Cho, M., H. M. Vaswani, T. Brixner, J. Stenger, and G. R. Fleming, 2005, J. Phys. Chem. B **109**(21), 10542.

Collini, E., C. Y. Wong, K. E. Wilk, P. M. G. Curmi, P. Brumer, and G. D. Scholes, 2010, Nature **463**(7281), 644.

Cresser, J. D., S. M. Barnett, J. Jeffers, and D. T. Pegg, 2006, Opt. Commun. **264**(2), 352.

Datta, A., and A. Shaji, 2008, Phys. Rev. Lett. **100**(5), 050502.

Egger, R., and C. H. Mak, 1994, Phys. Rev. B **50**(20), 15210.

Ekert, A. K., 1991, Phys. Rev. Lett. **67**(6), 661.

Engel, G. S., T. R. Calhoun, E. L. Read, T.-K. Ahn, T. Mancal, Y.-C. Cheng, R. E. Blankenship, and G. R. Fleming, 2007, Nature **446**(7137), 782.

Fassioli, F., and A. Olaya-Castro, 2010, New J. Phys. **12**(8), 085006.

Fenna, R. E., and B. W. Matthews, 1975, Nature **258**(5536), 573.

Ferraro, A., L. Aolita, D. Cavalcanti, F. M. Cucchietti, and A. Acín, 2010, Phys. Rev. A **81**(5), 052318.

Förster, T., 1948, Ann. Phys. **437**(1-2), 55.

Gaab, K. M., and C. J. Bardeen, 2004, J. Chem. Phys. **121**(16), 7813.

Galve, F., L. A. Pachón, and D. Zueco, 2010, Phys. Rev. Lett. **105**(18), 180501.

Gauger, E. M., E. Rieper, J. J. L. Morton, S. C. Benjamin, and V. Vedral, 2011, Phys. Rev. Lett. **106**(4), 040503.

Grover, L. K., 2001, Am. J. Phys **69**(7), 769.

Gühne, O., and G. Tóth, 2009, ArXiv e-prints **474**, 1.

Haken, H., and G. Strobl, 1973, Z. Phys **262**(2), 135.

Hayes, D., and G. S. Engel, 2011, Biophys. J. **100**(8), 2043.

Henderson, L., and V. Vedral, 2001, J. Phys. A - Math. Gen. **34**(35), 6899.

Hoyer, S., A. Ishizaki, and K. B. Whaley, 2011, ArXiv e-prints arXiv:1106.2911.

Hoyer, S., M. Sarovar, and K. Whaley, 2010, New J. Phys. **12**(6), 065041.

Huo, P., and D. F. Coker, 2010, J. Chem. Phys. **133**(18), 184108.

Ishizaki, A., and G. R. Fleming, 2009a, J. Chem. Phys. **130**(23), 234110.

Ishizaki, A., and G. R. Fleming, 2009b, J. Chem. Phys. **130**(23), 234111.

Joos, E., 2003, Decoherence and the appearance of a classical world in quantum theory, Springer, ISBN 9783540003908.

Koch, K., 2000, *Einführung in die Bayes-Statistik* (Springer), ISBN 9783540666707.

Kreisbeck, C., T. Kramer, M. Rodriguez, and B. Hein, 2011, J. Chem. Theory Comput **7**(7), 2166.

Leggett, A., and A. Garg, 1985, Phys. Rev. Lett. **54**(9), 857.

Louwe, R., J. Vrieze, A. Hoff, and T. Aartsma, 1997, J. Phys. Chem. B **101**(51), 11280.

May, V., and O. Kühn, 2011, *Charge and energy transfer dynamics in molecular systems* (John Wiley & Sons), ISBN 9783527407323.

Merali, Z., 2011, Nature **474**(7349), 24.

Modi, K., T. Paterek, W. Son, V. Vedral, and M. Williamson, 2010, Phys. Rev. Lett. **104**(8), 080501.

Mohseni, M., P. Rebentrost, S. Lloyd, and A. Aspuru-Guzik, 2008a, J. Chem. Phys. **129**(17), 174106.

Mohseni, M., P. Rebentrost, S. Lloyd, and A. Aspuru-Guzik, 2008b, J. Chem. Phys. **129**(17), 174106.

Mostame, S., P. Rebentrost, and D. I. Tsomokos, 2011, ArXiv e-prints arXiv:1106.1683.

Mülken, O., L. Mühlbacher, T. Schmid, and A. Blumen, 2010, Phys. Rev. E **81**(4), 041114.

Nalbach, P., J. Eckel, and M. Thorwart, 2010, New J. Phys. **12**(6), 065043.

Nalbach, P., A. Ishizaki, G. R. Fleming, and M. Thorwart, 2011, New J. Phys. **13**(6), 063040.

Olbrich, C., J. Strümpfer, K. Schulten, and U. Kleinekathöfer, 2010, J. Phys. Chem. B , 1.

Olbrich, C., J. Strümpfer, K. Schulten, and U. Kleinekathöfer, 2011, J. Phys. Chem. Lett. **2**(14), 1771.

Ollivier, H., and W. H. Zurek, 2001, Phys. Rev. Lett. **88**(1), 017901.

Owens, T., S. Webb, and L. Mets, 1987, Proc. Natl. Acad. Sci. USA **84**(6), 1532.

Panitchayangkoon, G., D. Hayes, K. Fransted, J. Caram, E. Harel, J. Wen, R. Blankenship, and G. Engel, 2010, Proc. Natl. Acad. Sci. USA **107**(29), 12766.

Plenio, M., 2005, Phys. Rev. Lett. **95**(9), 090503.

Plenio, M. B., and S. F. Huelga, 2008, New J. Phys. **10**(11), 113019.

Plenio, M. B., and S. Virmani, 2007, Quant. Inf. Comp. **7**, 1.

Rebentrost, P., R. Chakraborty, and A. Aspuru-Guzik, 2009, J. Chem. Phys. **131**(18), 184102.

Redfield, A. G., 1957, IBM J. Res. Dev. **1**(1), 19.

Ritschel, G., J. Roden, W. T. Strunz, and A. Eisfeld, 2011, ArXiv e-prints arXiv:1106.5259.

Sarovar, M., Y.-C. Cheng, and K. B. Whaley, 2011, Phys. Rev. E **83**(1), 011906.

Sarovar, M., A. Ishizaki, G. Fleming, and K. Whaley, 2010, Nature Phys. **6**(6), 462.

Scholak, T., F. d. Melo, T. Wellens, F. Mintert, and A. Buchleitner, 2011, Phys. Rev. E **83**(2), 021912.

Schrödinger, E., 1935, Math. Proc. Cambridge Phil. Soc. **31**, 555.

Sudarshan, E., 1977, J. Math. Phys. **18**, 756.

Tiersch, M., S. Popescu, and H. J. Briegel, 2011, ArXiv e-prints arXiv:1104.3883.

Vedral, V., 2010, Nature **468**(7325), 769.

Vedral, V., M. Plenio, M. Rippin, and P. Knight, 1997, Phys. Rev. Lett. **78**(12), 2275.

Weidemüller, M., 2009, Nature Phys. **5**(2), 91.

Weimer, H., M. Müller, I. Lesanovsky, P. Zoller, and H. P. Büchler, 2010, Nature Phys. **6**(5), 382.

Wen, J., H. Zhang, M. L. Gross, and R. E. Blankenship, 2009, Proc. Natl. Acad. Sci. USA **106**(15), 6134.

Werner, R., 1989, Phys. Rev. A **40**(8), 4277.

Wilde, M., J. McCracken, and A. Mizel, 2010, Proc. R. Soc. A **466**(2117), 1347.

Wootters, W. K., 1998, Phys. Rev. Lett. **80**(10), 2245.

Yu, T., and J. H. Eberly, 2009, Science **323**(5914), 598.

Zhang, W.-M., D. H. Feng, and R. Gilmore, 1990, Rev. Mod. Phys. **62**, 867.

A Appendix

A.1 The FMO Hamiltonian

$$H = \begin{pmatrix} 215 & -104.1 & 5.1 & -4.3 & 4.7 & -15.1 & -7.8 & 0 \\ -104.1 & 220 & 32.6 & 7.1 & 5.4 & 8.3 & 0.8 & 0 \\ 5.1 & 32.6 & 0 & -46.8 & 1 & -8.1 & 5.1 & 0 \\ -4.3 & 7.1 & -46.8 & 125 & -70.7 & -14.7 & -61.5 & 0 \\ 4.7 & 5.4 & 1 & -70.7 & 450 & 89.7 & -2.5 & 0 \\ -15.1 & 8.3 & -8.1 & -14.7 & 89.7 & 330 & 32.7 & 0 \\ -7.8 & 0.8 & 5.1 & -61.5 & -2.5 & 32.7 & 280 & 0 \\ 0 & 0 & 0 & 0 & 0 & 0 & 0 & 0 \end{pmatrix} \tag{A.1}$$

The Hamiltonian is taken from Adolphs and Renger (2006) and is used exhaustively in the community. The site energies and couplings are obtained by electrostatic calculations. The resulting optical spectra are in good agreement with experiments. The matrix elements are given in spectroscopic units (cm^{-1}). The diagonal elements (site energies) are shifted by 12230. In this units, $\hbar$ = 5.3 $\frac{\mathrm{ps}}{\mathrm{cm}}$. Therefore, the conversion to rates is achieved through a division by $\hbar$. We have extended the Hamiltonian by one dimension to include the reaction center. The ground state (no excitation) is not included explicitly. For this reason, the von-Neumann condition $\mathrm{tr}(\rho) = 1$ is not fulfilled. We equivalently use the condition $\rho_{00} = 1 - \mathrm{tr}(\rho)$, where ρ_{00} is the ground state population.

A.2 Note on the Validity of the Pure Dephasing Model

In order to know how far we can go with our very simple approach to couple the system to the environment, it would be desirable to compare it with a more sophisticated one.

Mülken *et al.* (2010) address the survival probability of an excitation on a dimer with trapping at one site within two different frameworks. The former is a Liouville-von-Neumann equation, which is closely related to the one we use. The ladder uses the Caldeira-Leggett model Caldeira and Leggett (1983) to describe the dimer-bath coupling and bath. The time evolution is then obtained by the numerically exact path integral Monte Carlo (PIMC) technique Egger and Mak (1994) which allows to see in which parameter regime the pure dephasing QME is appropriate and in which it fails.

The Lindblad term in Mülken *et al.* (2010) reads

$$\mathcal{L}(\rho) = -2\lambda \sum_j (\rho - \langle j| \rho |j\rangle) L_j, \tag{A.2}$$

where L_j are the Lindblad operators which are given by $L_j = |j\rangle \langle j|$. Comparing this to the dephasing term (3.6), we see that they coincide for $\gamma = \lambda$. The investigations show a perfect agreement of the Liouville-von-Neumann equation and PIMC at least up to $\gamma = \pi/4$ for site energies and couplings fixed at 1. Unfortunately, the next higher rate considered is $\gamma = 10\pi$ which deviates quite a lot. Nevertheless, since the ratio of the γ and the couplings matter, and the smallest coupling in the main transport pathways (see fig. 4.3) is on the order of $1\,\mathrm{ps}^{-1}$, we can *at least* assume that the model is valid for dephasing rates up to $\gamma = 1\,\mathrm{ps}^{-1}$. However, this is no justification for the model in order to describe the excitation transport in the FMO complex, since we do not know, if the system bath interaction in this case can be described within the model of Caldeira and Leggett.

A.3 Quantum Zeno Effect

Sudarshan (1977) pointed out that an unstable particle that is prepared in a specific state will stay in this state, if the particle is monitored continuously. In more general terms one can say that the time evolution of a quantum system can be stopped, if it is measured fast enough. This effect, known as *Quantum Zeno Effect*, is discussed exhaustively in the literature (e.g. Joos (2003)). In the context of our work, however, it is important to note that a recurring measurement operation can be identified with the action of the pure dephasing Lindbladoperator. Based on Cresser *et al.* (2006), this will be shown in the following.

A.3.1 Pure Dephasing as a Measurement

Let the A_i be projective measurement operators. The density matrix ρ immediately after a measurement has the form

$$\rho(t) \to \rho(t+\epsilon) = \sum_i A_i \rho(t) A_i^\dagger. \tag{A.3}$$

If the evolution is not perturbed by a measurement, the density matrix will be

$$\rho(t) \to \rho(t+\epsilon) = \rho(t) - \frac{i}{\hbar}[H, \rho(t)]\epsilon. \tag{A.4}$$

The average evolution is then given by the weighted sum

$$\rho(t) \to \rho(t+\epsilon) = (1-\gamma)\rho(t) - \frac{i}{\hbar}[H, \rho(t)]\epsilon + \gamma \sum_i A_i \rho(t) A_i^\dagger, \tag{A.5}$$

where we have taken only terms linear in ϵ and γ is the average rate at which the measurement is performed. In the limit $\epsilon \to 0$, we end up with a QME in Lindblad form

$$\frac{\partial \rho}{\partial t} = -\frac{i}{\hbar}[H, \rho] + \gamma(\sum_i A_i \rho(t) A_i^\dagger - \rho) \tag{A.6}$$

Next, we specify the A_i to be projectors on the state $|i\rangle$

$$A_i = A_i^\dagger = |i\rangle \langle i|, \tag{A.7}$$

and insert them into the QME (A.6)

$$\frac{\partial \rho}{\partial t} = -\frac{i}{\hbar}[H, \rho] + \gamma(\sum_i \rho_{ii} \left|i\right\rangle \left\langle i\right| - \rho). \tag{A.8}$$

If we compare the last term with the pure dephasing Lindbladoperator (3.5)

$$\mathcal{L}_{deph}(\rho) = \gamma \sum_i [A_i \rho A_i^\dagger - \frac{1}{2}\{A_i A_i^\dagger, \rho\}] \tag{A.9}$$

$$= \gamma \sum_i [\rho_{ii} \left|i\right\rangle \left\langle i\right| - \rho \left|i\right\rangle \left\langle i\right|] \tag{A.10}$$

$$= \gamma(\sum_i \rho_{ii} \left|i\right\rangle \left\langle i\right| - \rho \sum_i \left|i\right\rangle \left\langle i\right|) \tag{A.11}$$

$$= \gamma(\sum_i \rho_{ii} \left|i\right\rangle \left\langle i\right| - \rho), \tag{A.12}$$

we see that the effect of pure dephasing can be interpreted as a measurement with rate γ.

A.4 Optimal Basis for Projective Measurement

We define

$$f(\theta,\phi) = p_1(\theta)S(\rho_{A|\Pi_1^B}(\theta,\phi)) - p_2(\theta)S(\rho_{A|\Pi_2^B}(\theta,\phi)), \tag{A.13}$$

where the angles ϕ and θ are hidden in the projective measurement operators $\Pi_i^B(\theta,\phi)$ and the normalization factors $p_i(\theta)$. The ϕ-dependence vanishes because we assume no coherences between the zero- and single-excitation subspaces. Then $f(\theta,\phi) = f(\theta)$. The position, but not the value, of the minima of $f(\theta)$ are independent of the time point at which the density matrix is evaluated and independent of the dephasing rate. An exemplary plot, with A=1,2, B=3, t=0.1 and γ=0 is shown in fig. A.1. The edges at $\theta = n\pi$ are numerical artifacts because $0 \cdot S(0)$ appears. If this is correctly interpreted as zero, all minima coincide, and $\theta^* = \frac{n\pi}{2}$. Therefore, the optimal basis leads to a projective measurement onto the ground and excited state of subsystem B.

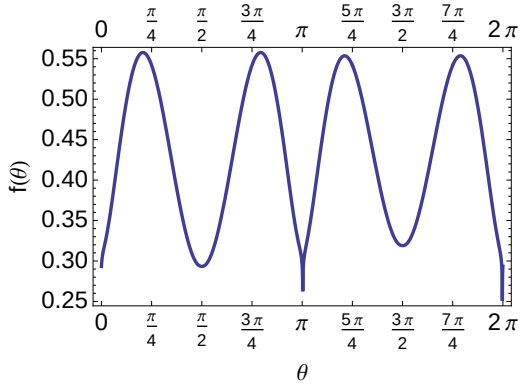

Figure A.1: The minimum of the function $f(\theta)$ appears in the definition of Quantum Discord. The locations of the minima are at $\theta^* = \frac{n\pi}{2}$.

B Lists

B.1 List of Figures

Erklärung:

Ich versichere, dass ich diese Arbeit selbstständig verfasst habe und keine anderen als die angegebenen Quellen und Hilfsmittel benutzt habe.

Heidelberg, den 28.09.2011 . . . . . .